AD-A015 240

EXPERIMENTS ON LARGE PLASTIC DEFORMATIONS OF CIRCULAR PLATES WITH WORK HARDENING

Robert Winter, et al

Grumman Aerospace Corporation
Bethpage, New York

July 1975

DISTRIBUTED BY:

NTIS
National Technical Information Service
U. S. DEPARTMENT OF COMMERCE

RE-502

EXPERIMENTS ON LARGE PLASTIC DEFORMATIONS OF CIRCULAR PLATES WITH WORK HARDENING

July 1975

RESEARCH DEPARTMENT

DDC
RECEIVED
OCT 7 1975
C

Reproduced by
NATIONAL TECHNICAL
INFORMATION SERVICE
US Department of Commerce
Springfield, VA. 22151

DISTRIBUTION STATEMENT A
Approved for public release;
Distribution Unlimited

GRUMMAN AEROSPACE CORPORATION
BETHPAGE NEW YORK

Unclassified

Security Classification

DOCUMENT CONTROL DATA - R & D

(Security classification of title, body of abstract and indexing annotation must be entered when the overall report is classified)

1 ORIGINATING ACTIVITY *(Corporate author)* Grumman Aerospace Corporation	2a. REPORT SECURITY CLASSIFICATION Unclassified 2b. GROUP N/A

3 REPORT TITLE
Experiments on Large Plastic Deformations of Circular Plates with Work Hardening

4 DESCRIPTIVE NOTES *(Type of report and inclusive dates)*
Research Report

5 AUTHOR(S) *(First name, middle initial, last name)*
Robert Winter
Howard S. Levine

6 REPORT DATE July 1975	7a. TOTAL NO. OF PAGES 83	7b. NO. OF REFS 28
8a. CONTRACT OR GRANT NO b. PROJECT NO c. N/A d.	9a. ORIGINATOR'S REPORT NUMBER(S) RE-502 9b. OTHER REPORT NO(S) *(Any other numbers that may be assigned this report)* None	

10 DISTRIBUTION STATEMENT
Approved for public release; distribution unlimited

11 SUPPLEMENTARY NOTES None	12. SPONSORING MILITARY ACTIVITY None

13 ABSTRACT
Tests were performed on three simply supported circular plates of aluminum alloy 2024-0, under a central concentrated load, with large deflection. The load was provided by a small diameter hard steel rod. Measurements were made of load, deflections, and strains, and membrane and bending strains were calculated from the test data. Twenty electrically bonded strain gauges were used to measure the distribution of radial and circumferential strain components along a radial line on both faces of each plate. The test data are presented in comparison with theoretical predictions generated by the Grumman-developed finite element computer code PLANS. The correlation between theory and test data was excellent for deflections, and generally good for strains, using the circular line load predictions. The uniform pressure case slightly overpredicted the central deflections and greatly overpredicted the peak strains. The greatest deviation between predicted and measured strains was in the region of the concentrated load, where local transverse normal and shear stresses are not included in the theory, and where the errors caused by the assumed load distribution would be maximum. The plates exhibited initial loss of stiffness under the plastic bending behavior, followed b a rapidly increasing membrane action resulting from large deflections, which provided much additional resistance to the applied load.

DD FORM 1 NOV 65 1473

Unclassified

Security Classification

Grumman Research Department Report RE-502

EXPERIMENTS ON LARGE PLASTIC DEFORMATIONS OF CIRCULAR PLATES WITH WORK HARDENING

by

R. Winter

and

H. S. Levine

Materials and Structural Mechanics

July 1975

Approved by: Charles E. Mack, Jr.
Charles E. Mack, Jr.
Director of Research

1a

DISTRIBUTION STATEMENT A
Approved for public release;
Distribution Unlimited

SUMMARY

Tests were performed on three simply supported circular plates of aluminum alloy 2024-0, under a central concentrated load, with large deflection. The load was provided by a small diameter hard steel rod. Two plates, having a diameter-to-thickness ratio of $D/h = 40.6$, were loaded to a central deflection of 2.6 times the thickness, and one plate of $D/h = 20.0$ was loaded to a central deflection of 1.6 times the thickness. Measurements were made of load, deflections, and strains, and membrane and bending strains were calculated from the test data. Twenty electrically bonded strain gauges were used to measure the distribution of radial and circumferential strain components along a radial line on both faces of each plate. The test data are presented in comparison with theoretical predictions generated by the Grumman-developed finite element computer code PLANS. The theoretical model used two different assumed distributions of contact pressure under the loading rod to approximate the test load distribution. They were a uniform contact pressure and a concentrated line load along the rod edge circle. The correlation between theory and test data was excellent for deflections, and generally good for strains, using the circular line load predictions. The uniform pressure case slightly overpredicted the central deflections and greatly overpredicted the peak strains. The greatest deviation between predicted and measured strains was in the region of the concentrated load, where local transverse normal and shear stresses are not included in the theory, and where the errors caused by the assumed load distribution would be maximum. The plates exhibited initial loss of stiffness under the plastic bending behavior, followed by a rapidly increasing membrane action resulting from large deflections, which provided much additional resistance to the applied load.

TABLE OF CONTENTS

Section		Page
1.	Introduction	1
2.	Procedure	4
	Test Specimens	4
	Plate Tests	7
	Material Properties Tests	20
3.	Data	22
	Material Properties	22
	Plate Behavior	30
4.	Conclusions	63
5.	References	66
Appendices:		
	A. Strain Gauge Configurations	69
	B. Strain Gauge Data Processing	71
	C. True Stress Calculations	78
	D. Theoretical Model	80

LIST OF FIGURES

Figure		Page
1	Typical Specimen Layout and Numbering Scheme	5
2	Tension Coupon Dimensions	6
3	Close-up View of Plate Experiment	9
4	Over-all View of Plate Experiment	10
5	Close-up View of Plate Fixture and Displacement Transducers	11
6	Strain Gauge Layout and Numbering Scheme	14
7	Typical Strain Gauge Installation, Upper Surface	15
8	Typical Strain Gauge Installation, Lower Surface	16
9	Typical Tension Coupon	20
10	Typical Load-Extension Record	23
11	Typical Strain Gauge Data	24
12	Average Stress-Strain Curve for $\frac{1}{8}$-inch Plate Material	25
13	Average Stress-Strain Curve for $\frac{1}{4}$-inch Plate Material	26
14	Deflection History, Plate 1A125	32
15	Circumferential Strain History, Plate 1A125	35
16	Radial Strain History, Plate 1A125	36
17	Circumferential Strain Distributions, Lower Surface, Plate 1A125	37
18	Radial Strain Distributions, Lower Surface, Plate 1A125	38

Figure		Page
19	Symmetry of Strain Data, Plate 1A125	41
20	Deflection History, Plate 4A125	43
21	Circumferential Strain History, Plate 4A125	45
22	Circumferential Strain Distributions, Lower Surface, Plate 4A125	46
23	Radial Strain Distributions, Lower Surface, Plate 4A125	47
24	Symmetry of Strain Data, Plate 4A125	49
25	Circumferential Bending and Membrane Strain Distributions, Plate 4A125	50
26	Deflection History, Plate 4A250	53
27	Circumferential Strain History, Plate 4A250	55
28	Radial Strain History, Plate 4A250	56
29	Circumferential Strain Distributions, Lower Surface, Plate 4A250	57
30	Radial Strain Distributions, Lower Surface, Plate 4A250	58
31	Symmetry of Strain Data, Plate 4A250	59
32	Circumferential Membrane Strain Distribution, Plate 4A250	60
33	Circumferential Bending Strain Distribution, Plate 4A250	61
B-1	Strain Gauge Error, After Certain Corrections ...	73
B-2	Strain Gauge Alignment Geometry	75

Figure		Page
B-3	Mohr's Circle for Strain Gauge Alignment Error Analysis	75
D-1	Finite Element Models for Plates	82

1. INTRODUCTION

A series of tests were performed for the purpose of exhibiting details of the plastic bending characteristics of a representative structural element and to evaluate the predictive capability of the AXSHEL (Axisymmetric Shell Analysis) module of the Grumman-developed PLANS (Plastic Large Deflection Analysis of Structures) system of computer codes.

The simply supported circular plate under a central concentrated load was chosen for these purposes because it is one of the simplest structural elements exhibiting a biaxial stress state in bending. The simple loading and geometry would allow for easy fabrication and fixturing, while the load concentration would provide a severe test of the theory because of the large strain gradients and contact stresses. The material chosen was 2024-0 (annealed) aluminum alloy, which has a very small elastic strain range and a large plastic strain before failure, thereby allowing large plastic strains to be developed at relatively low loads. It has a gradually changing tangent modulus in the plastic strain range, which is more typical for aerospace-type materials than the abrupt yielding with zero plastic tangent modulus (to 2 or 3 percent strain) exhibited by the mild steel used in most previously reported tests.

The tests were required to provide data on the distribution of strain components and the deflections. This is because the deflections reflect an integrated behavior of all points in the structure, and the transverse motion of any local point is therefore a somewhat gross measure of the structural response. The local strains, however, are much more dependent on purely local behavior,

and thus examination of the strain distribution over the structure can provide more information on the variation of structural behavior from point to point.

While there has been a moderate amount of test data available to verify various elastic-plastic analysis methods (Refs. 1 through 19), most reports show only deflections but do not report strain distributions. The notable exceptions are tests by Ohashi and Murakami (Refs. 13 and 14), Ohashi and Kawashima (Ref. 16), and May (Ref. 15) for the moderate thickness range of mild steel plates. Cooper and Shifrin (Ref. 6) reported strains and curvatures only near the edge of very thin mild steel plates, for which the membrane behavior was dominant. Some earlier documents (Refs. 2 and 3) by Ramberg, McPherson, and Levy reported residual deformation and strain data on very thin aluminum, magnesium, and stainless steel plates. They applied the load cyclically, increasing the peak load after each release, so that the usual monotonically increasing stress-strain data does not apply. The flow patterns are of additional interest, as reported by Lance and Onat (Ref.12). Recently, Durelli, Parks, and Chen (Ref. 19) have reported deformations and strains for a centrally loaded thick plate (D/h = 6). They used the Moire optical strain measuring method, as well as the usual bonded resistance strain gauges. However, their large plate thickness would make the shear stresses too prominent for comparison with the AXSHEL bending and membrane theory. One of the most interesting tests on mild steel was that of Sherbourne and Srivastava (Ref. 18) who carried the load level high enough to exhibit initial plastic softening under bending action, restiffening under increasing membrane action, and a second plastic softening. But, unfortunately, they did not report any strain data.

In summary, no test data were found for both deflections and strains on plates of a gradually yielding, work hardening material exhibiting combined bending and membrane action. The available reported test data were considered inadequate for the stated purposes, so a related test program was undertaken, as follows.

2. PROCEDURE

Test Specimens

Experiments were performed on three 5.35-inch diameter flat circular plate specimens, two of which were $\frac{1}{8}$-inch nominal thickness and one of $\frac{1}{4}$-inch nominal thickness. The material stress-strain curves were determined by tests on 16 tension coupons, composed of 8 coupons for each thickness, and two compression coupons for the $\frac{1}{8}$-inch plates.

It was decided to make the specimens from aluminum alloy 2024-0 (annealed), because its low yield strength at room temperature would produce large plastic strains at small loads. Also important was its reported isotropy and nearly equal tension and compression properties. After examining a number of candidate 4 by 8 foot plates, plates of $\frac{1}{8}$-inch and of $\frac{1}{4}$-inch nominal thickness were selected with clean, unmarred surfaces, and a 2-foot square section was cut from each. Four circular plate blanks, and 12 tension coupon blanks were saw-cut from this square plate, following the pattern shown in Fig. 1.

The plate specimens and tension coupons were machined on their edges only, leaving the original face surfaces intact. The plate specimens were finished to a nominal 5.35-inch diameter. The final tension coupon dimensions are shown in Fig. 2. The plates and tension coupons were marked on the edges to keep track of their numbers according to the layout of Fig. 1. The scrap material remaining from the original plates was saved, and was used later in the project to make $\frac{1}{4}$- and $\frac{1}{8}$-inch diameter by 1-inch long cylindrical compression coupons.

In summary, no test data were found for both deflections and strains on plates of a gradually yielding, work hardening material exhibiting combined bending and membrane action. The available reported test data were considered inadequate for the stated purposes, so a related test program was undertaken, as follows.

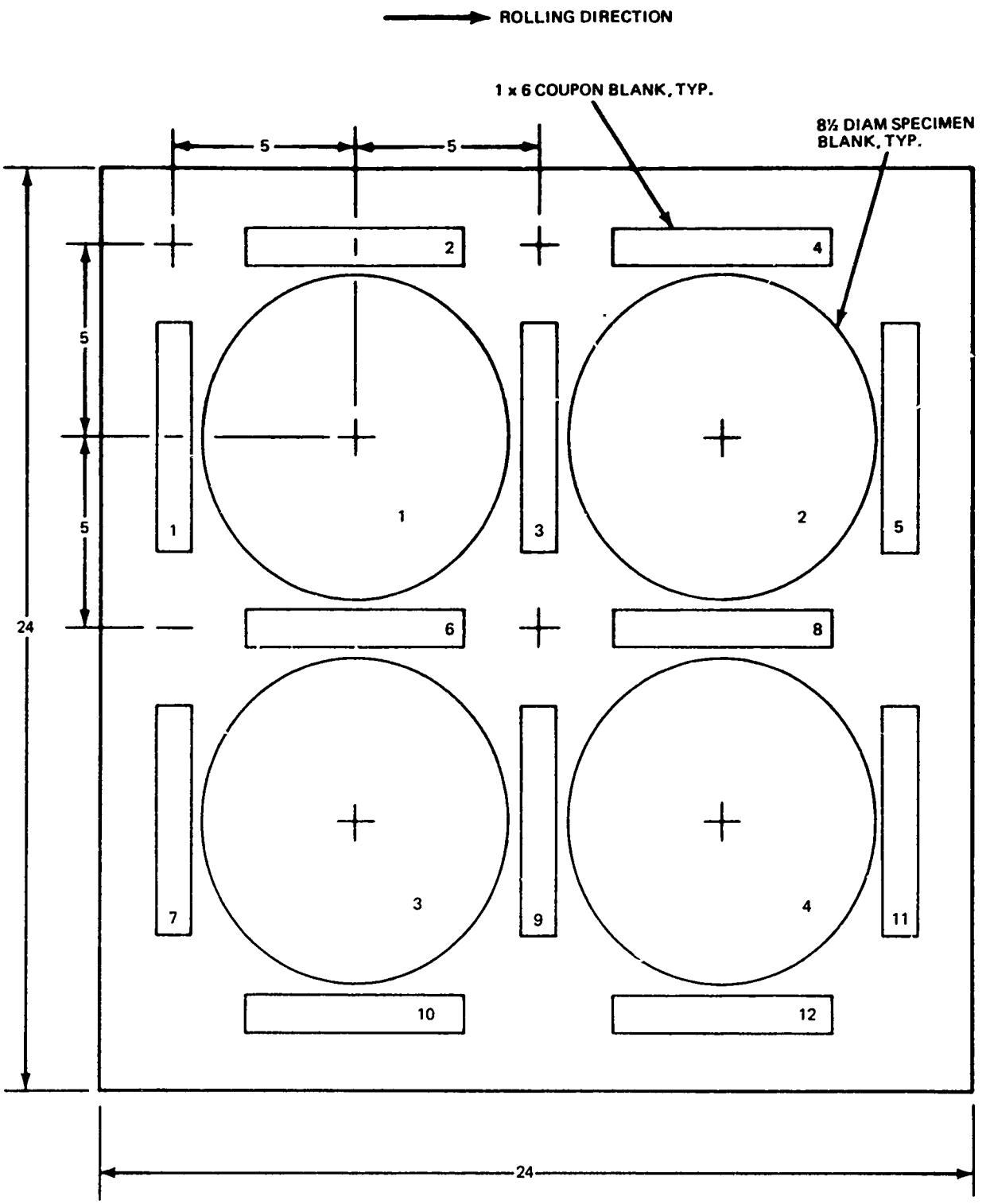

Fig. 1. Typical Specimen Layout and Numbering Scheme

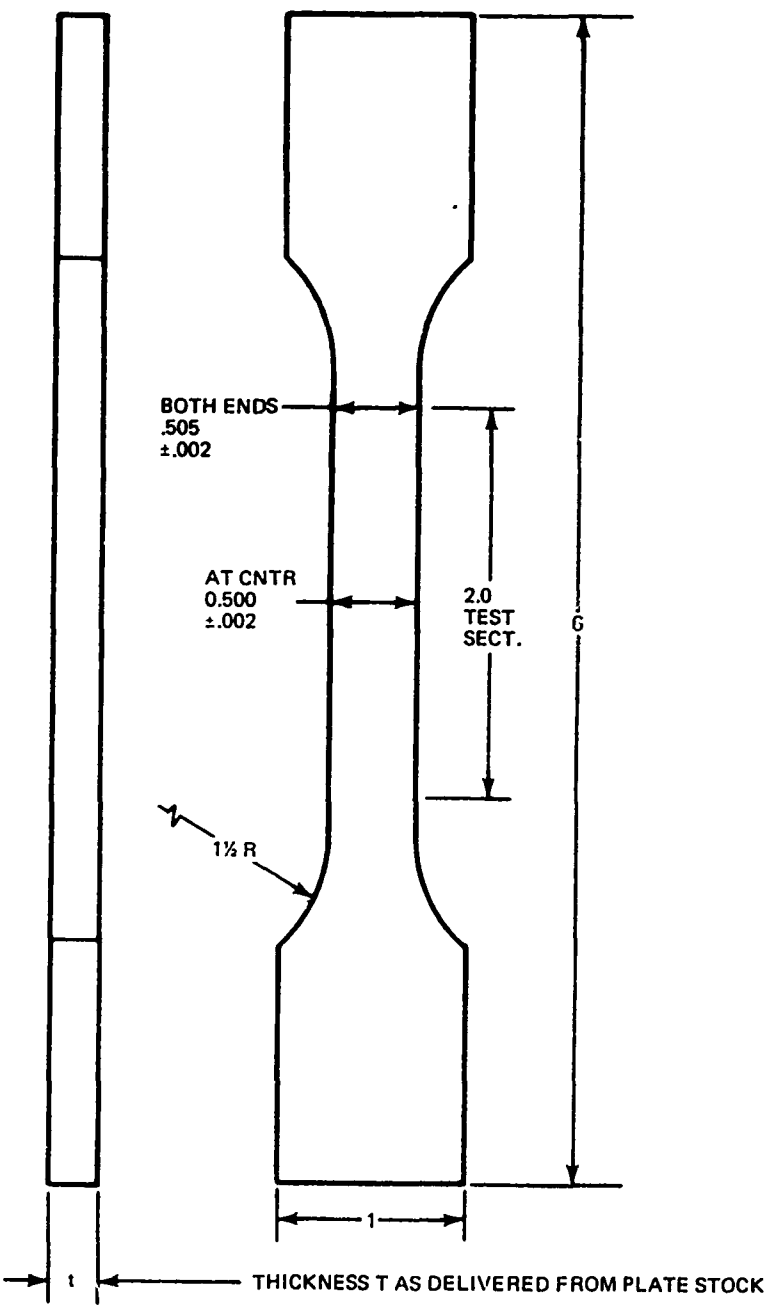

Fig. 2. Tension Coupon Dimensions

Although a total of 8 plate blanks were cut from the $\frac{1}{8}$- and $\frac{1}{4}$-inch plate stock, only four circular plate specimens, numbered 1 and 4 of each thickness, were finish machined and instrumented at this time. Of these four, specimen number 1A250 (number 1 of 0.250-inch nominal thickness) was not tested at this time. Thus, only three plate specimens, composed of two $\frac{1}{8}$-inch plates (1A125 and 4A125) and one $\frac{1}{4}$-inch plate (4a250), are reported on. Only those tension coupon blanks immediately adjacent to plate blanks 1 and 4 were machined into finished tension coupons. These are the 8 blanks of each thickness numbered 1, 2, 3, 6, 8, 9, 11, and 12 in Fig. 1.

Plate Tests

After each circular plate specimen was finished, it was carefully measured to determine its diameter, thickness variation, and deviation from flat. These measurement data are listed in Table 1, for the three plates reported here.

The plate test arrangement is shown in Figs. 3, 4, and 5. The plate specimen (1), rested on the hard steel support fixture (2), which was installed on the lower crossbeam (3) of the testing machine frame. The testing machine was an Instron Model TTDL, a screw-driven, constant crosshead speed machine with a 20,000 pound load capacity. The loading rod (4) was attached to the load cell (5), which was mounted to the underside of the moving crossbeam (6), (see Fig. 4). The testing machine control console (7) also contained the load cell conditioner and recording chart. The cabinet on the right housed the strain gauge conditioning and recording equipment, including a 20-channel scanner/indicator (8), and a digital printer (9). To the left of the plate specimen were the

TABLE 1 PLATE MEASUREMENTS SUMMARY

Plate No.	Diameter, Inches ± 0.001		Thickness, Inches ± 0.0002											Flatness Deviation	
	A-C	B-D	A	B	C	D	E	F	G	H	I	Avg	Average Deviation	A-C	B-D
1A-125	5.350	5.349	0.1287	0.1283	0.1281	0.1284	0.1284	0.1283	0.1281	0.1285	0.1281	0.1283	± 0.00016	0.030 Concave	0.002 Concave
4a-125	5.347	5.347	0.1287	0.1285	0.1286	0.1286	0.1287	0.1284	0.1286	0.1286	0.1286	0.1286	± 0.00006	–	–
4A-250	5.346	5.346	0.2614	0.2616	0.2614	0.2616	0.2614	0.2616	0.2615	0.2615	0.2615	0.2615	± 0.00007	0.002 Concave	–

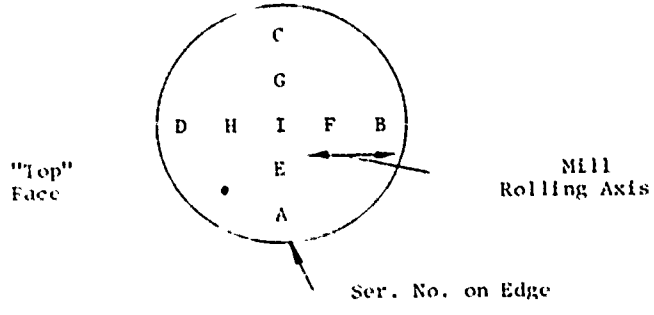

Measurement Pattern

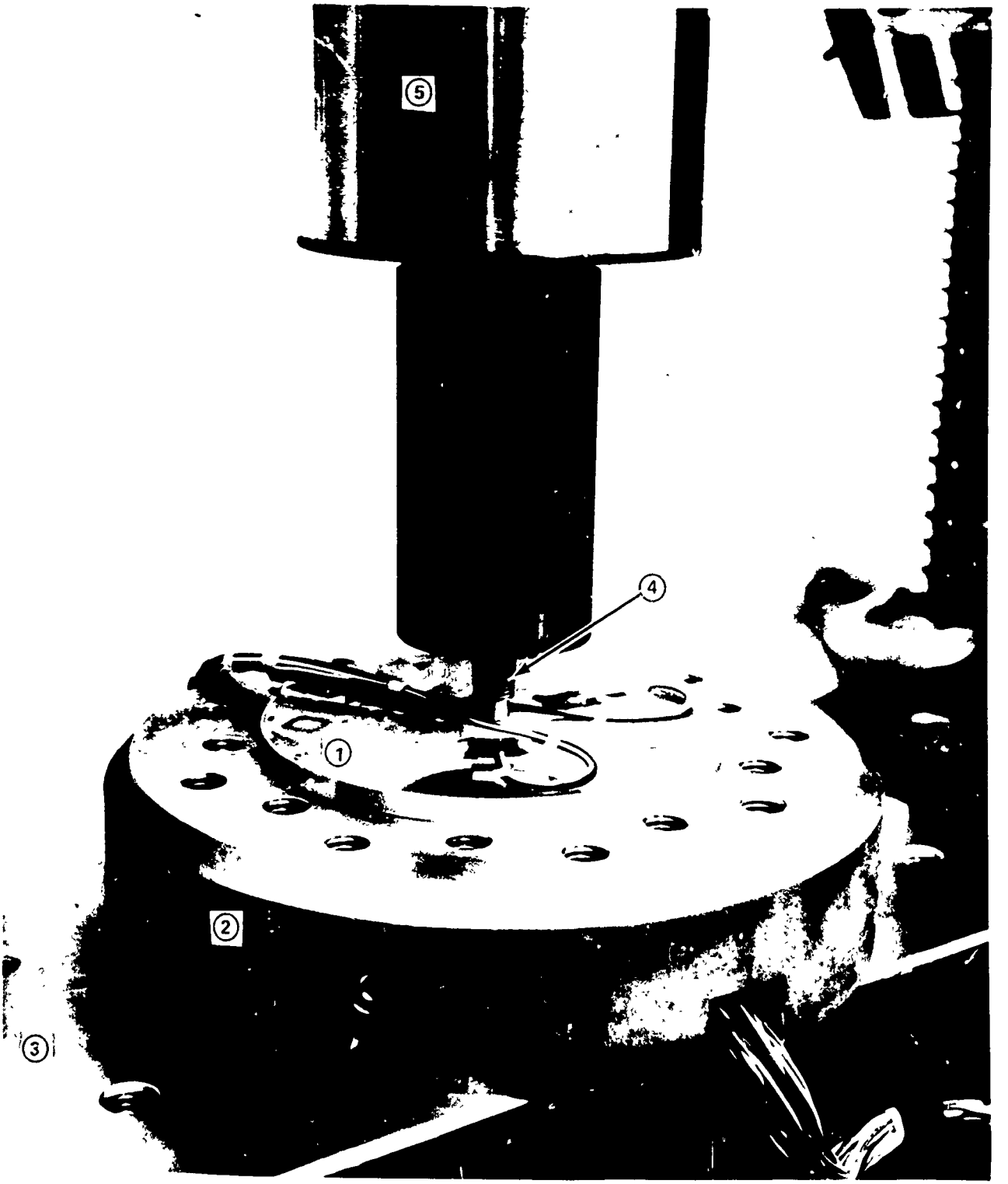

Fig. 3. Close-Up View of Plate Experiment

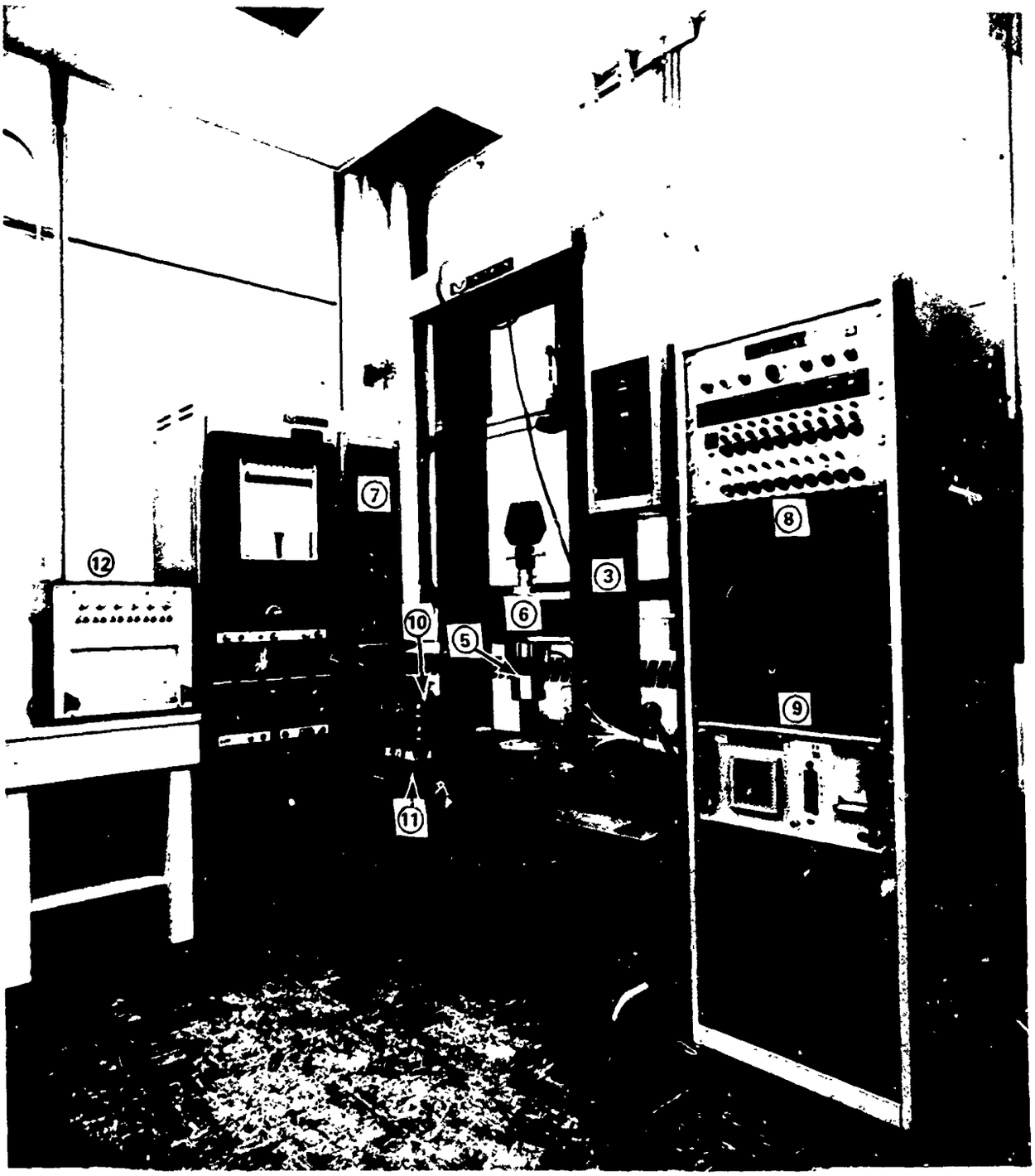

Fig. 4. Over-all View of Plate Experiment.

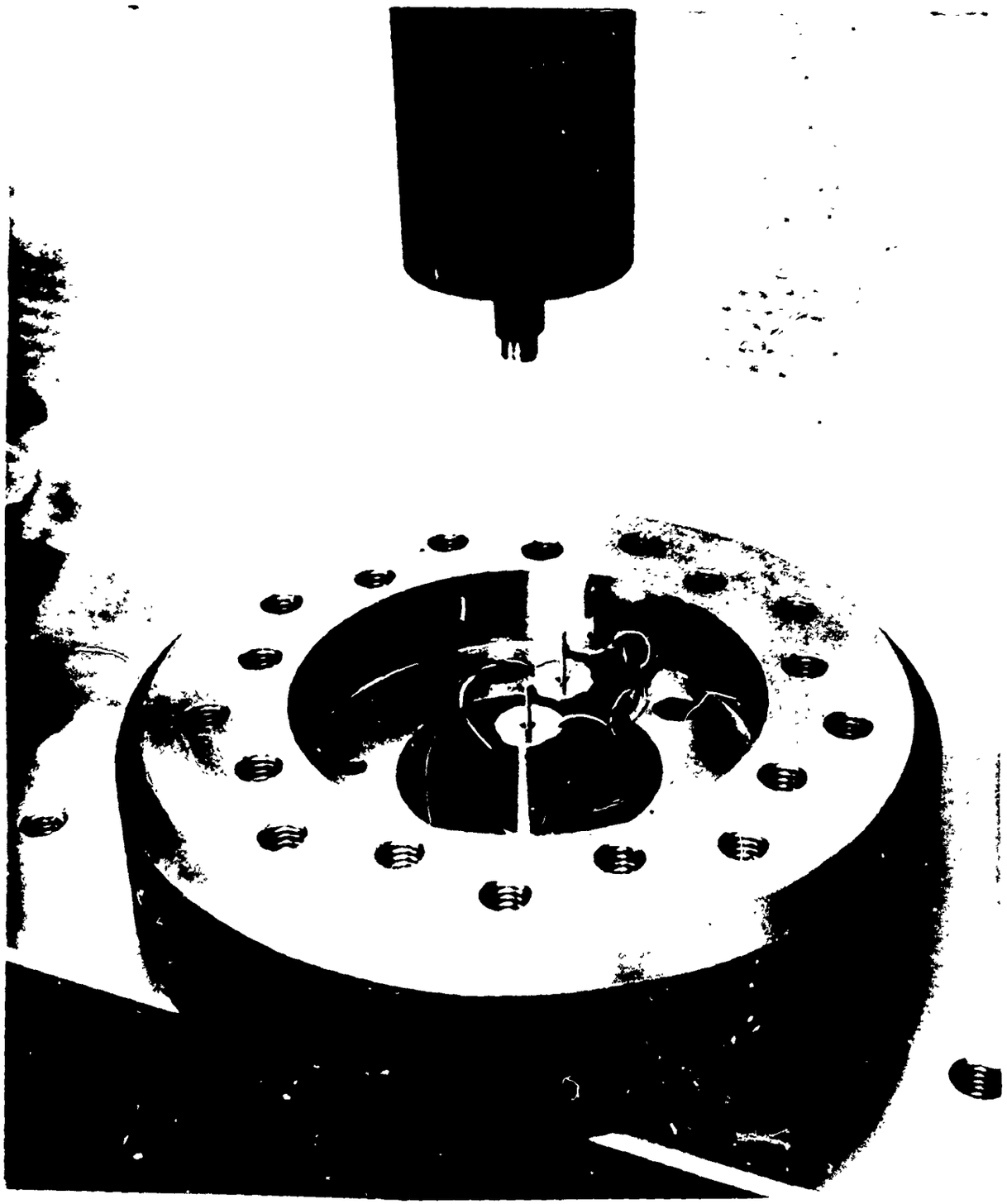

Fig. 5. Close-Up View of Plate Fixture and Displacement Transducers

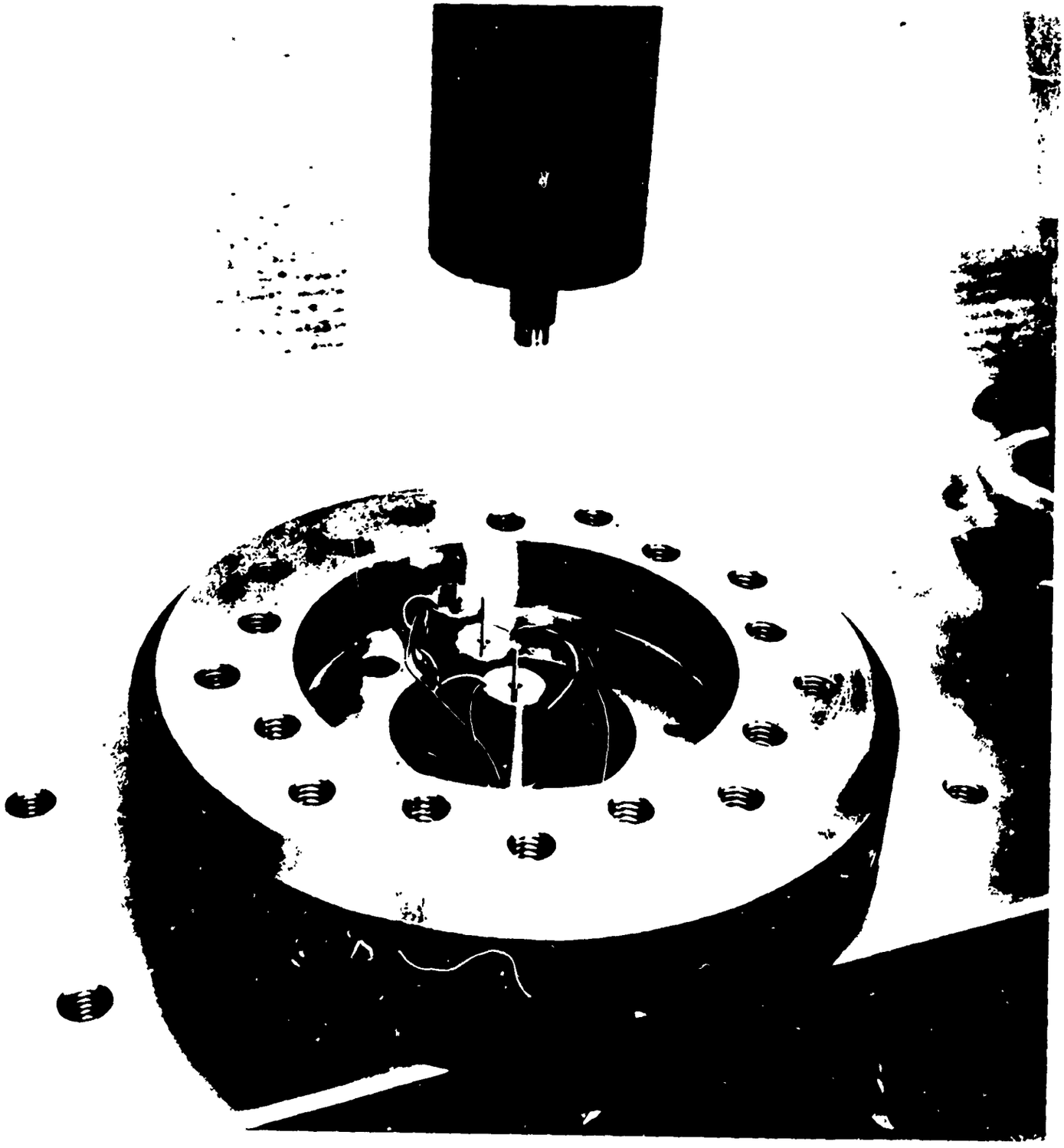

Fig. 9. Close-Up View of Plate Fixture and Displacement Transducers

Linear Variable Differential Transformer (LVDT) deflection transducer conditioning and recording units, including the dc power supplies (10), a signal balancing unit (11), and a strip-chart recorder (12).

A closeup view appears in Fig. 5 of the plate support fixture, the three LVDT displacement transducers, and the loading rod attached to the load cell. These are shown in position prior to the installation of the plate specimen. The fixture opening was 5.22-inches in diameter, supporting the plate specimens of 5.35-inch nominal diameter. The hardened steel loading rod was initially 0.430-inch in diameter for plate No. 1A125, and was then reduced to 0.375 inch for the remaining two plates.

The instrumentation used in the plate tests were 3 LVDT deflection transducers, 21 surface-bonded strain gauges, and one load cell.

The three LVDT's are shown in place in Fig. 5, and were the dc in-dc out type (Tresco Inc.) with built-in oscillator and rectifier, a 0.10-inch linear range, and a 0.20-inch usable range. The LVDT's were located on a radial line at nominal positions of 0, 1, and 2 inches from the center of the support fixture. The contact tip on the probe of the centerline LVDT was flat, to pick up the peak deflection of the center of the plate, while the other two probe tips were sharp-pointed, to remain in constant touch with their initial contact points on the plate bottom. The LVDT's were supplied with 24 volts regulated dc power; the output signals were sent to a potentiometer box that balanced the starting signals to zero and then sent to the strip chart recorder.

Motion of the load rod tip was also used as a source of deflection data. This was done by relating the known constant crossbeam speed to the known constant speed of the Instron chart recording the load, and then adjusting for the calibrated deflection versus load characteristics for the machine in that particular configuration.

The strain gauge layout for the plates is shown in Fig. 6 and a typical gauge installation is shown in Figs. 7 and 8. The upper surface was defined as the surface contacted by the loading rod. Gauges 2 through 17 were 90 degree dual-element type (FAET-12D-12S13ET, BLH Electronics Inc.) and gauges 1 and 18-21 were single-element type (FAE-12S-12S13ET, BLH Electronics Inc.), all of the same lot number (A270). These are foil gauges sandwiched between polyimide carrier and cover strips, with factory-attached copper terminals, a $\frac{1}{8}$-inch square sensing grid, a 120-ohm nominal resistance, and a thermal expansion rate of 13.0×10^{-6} per °F. The manufacturer's data show a thermally induced strain error of -10 microstrain or less on aluminum, and a gauge factor change of ±0.2 percent or less, both between 50 and 125°F.

This type of gauge configuration was selected after an exploratory test series, described in Appendix A. These tests showed that such gauges could survive almost as much peak strain as the traditional handmade wire jumper gauge configuration, with much less installation effort.

The bridge circuit was the single active arm type with two lead wires, with the nonlinearity effect compensated by data processing. The bridge excitation was 5 volts. The strain gauges were placed so that both the radially and circumferentially oriented gauges of a pair would be located at the same radius. This caused

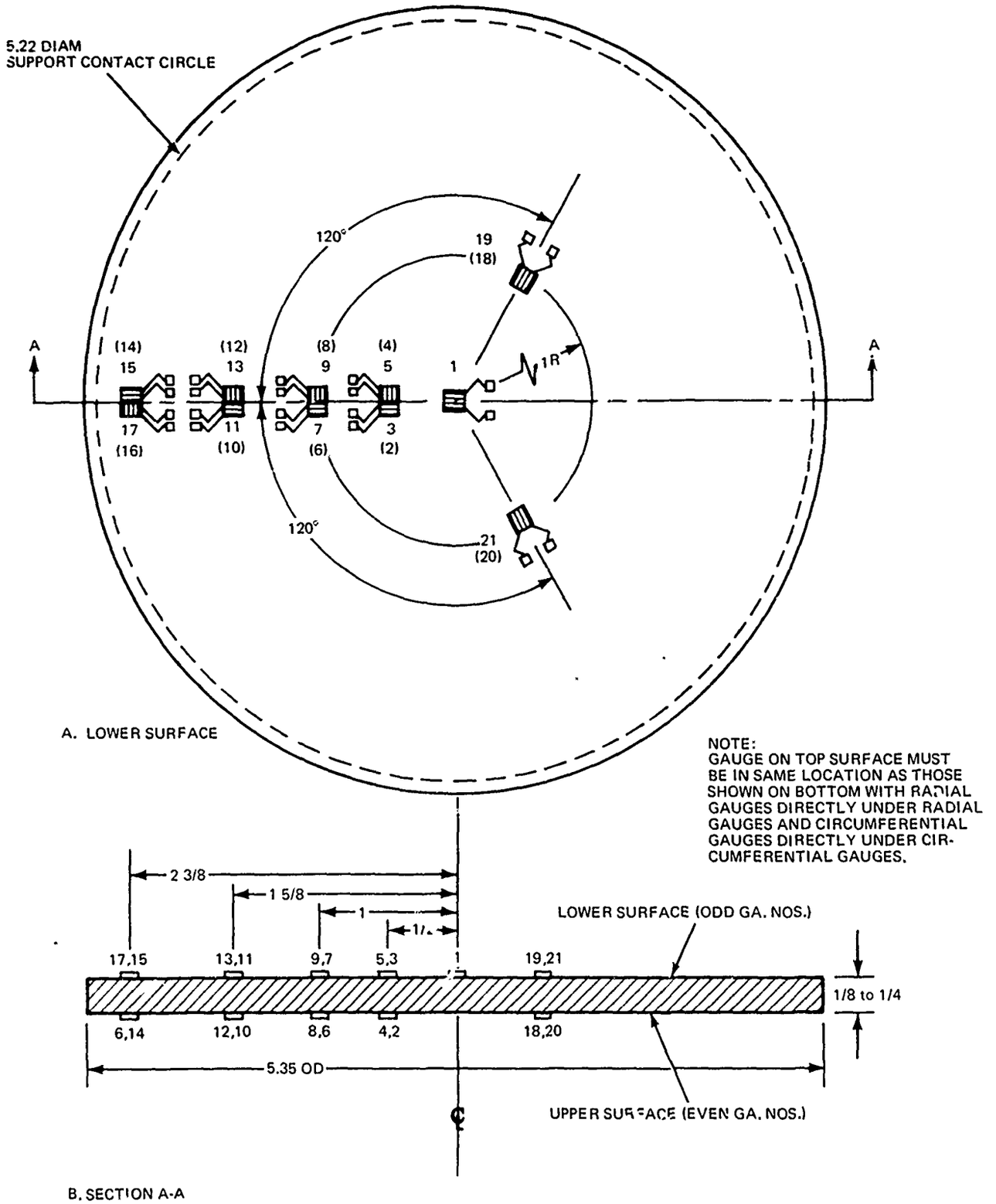

Fig. 6. Strain Gage Layout and Numbering Scheme

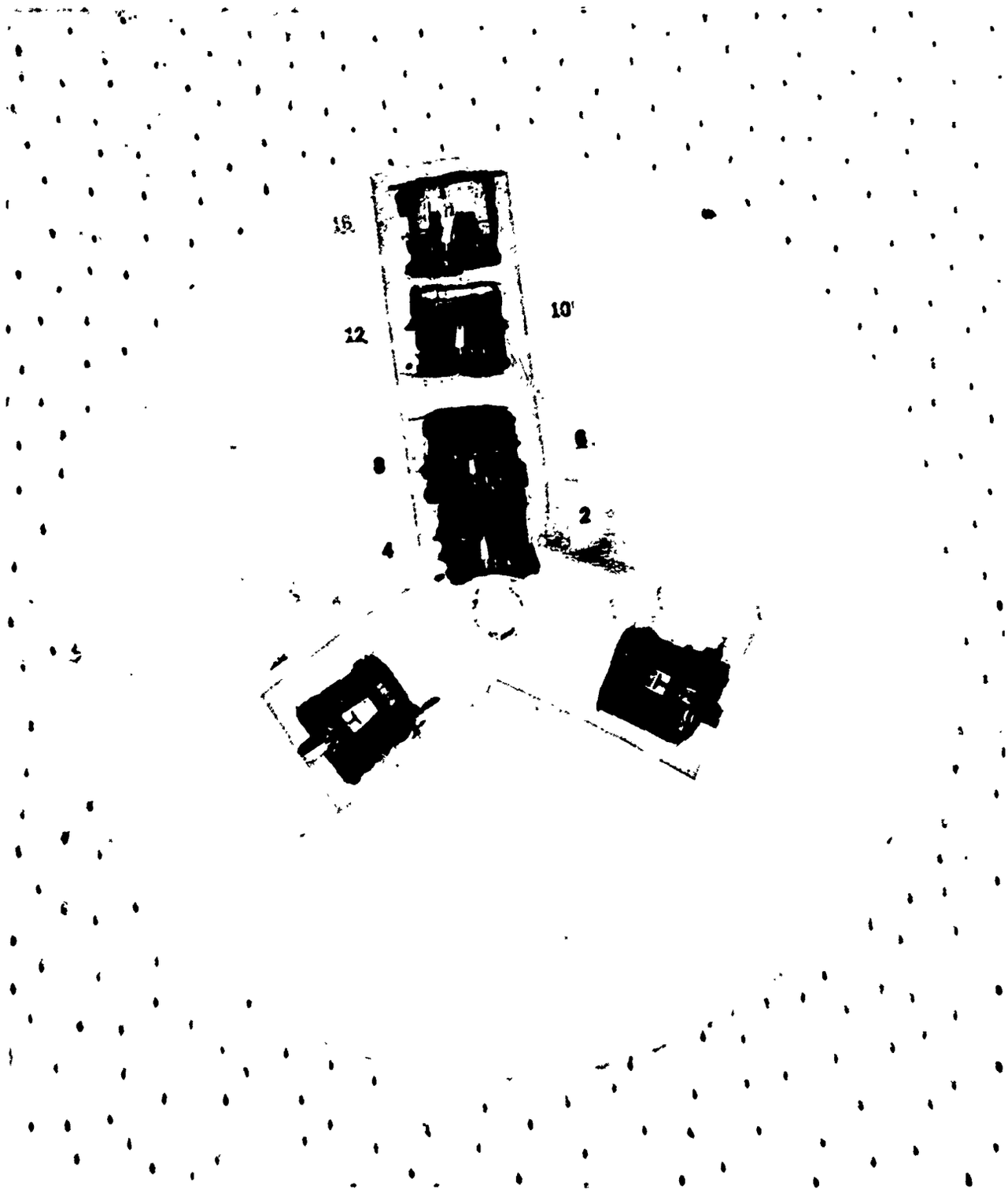

Fig. 7. Typical Strain Gauge Installation, Upper Surface

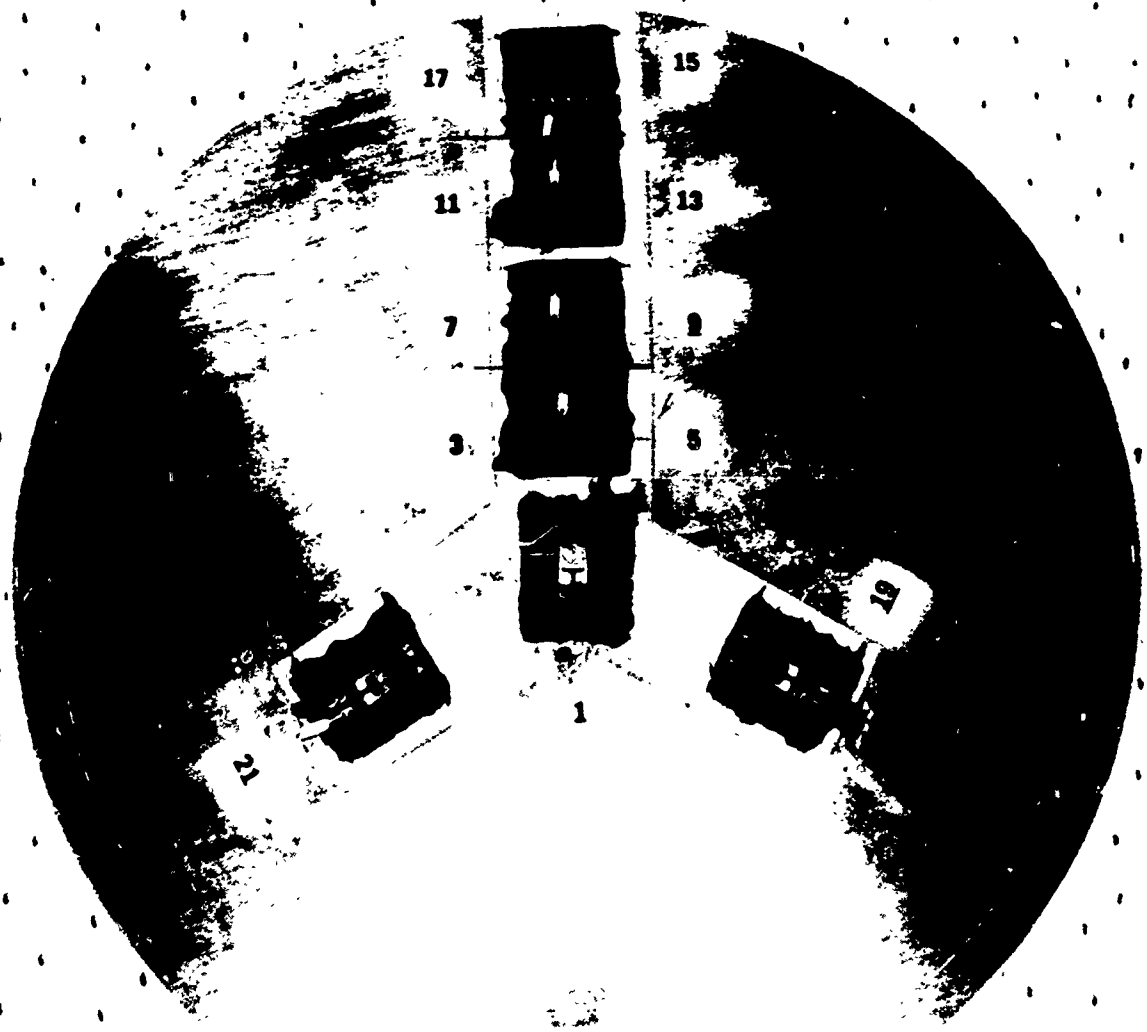

Fig. 8. Typical Strain Gauge Installation, Lower Surface

the gauges to be rotated slightly with respect to the radial and circumferential axes through the gauge centers. The effect of this was corrected in the data processing. The dual-gauge sets provided for strain measurements mutually perpendicular to each gauge, thus permitting transverse gauge error to be corrected in data processing. The various gauge correction procedures are described in Appendix B.

Specimen surfaces were roughened lightly by an abrasive powder blast in the areas to receive the strain gauges, with an associated thickness reduction of less than 0.0002 inch. The gauges were then bonded to the surface using a two-part epoxy cement (GA-2, Automation Industries Inc.), cured at 79-80°F for a minimum of 12 hours under clamping pressure. The manufacturer states a 20 percent maximum usable strain at room temperature for this cement.

The load cell was a stiff axial rod strain-gauged type (Instron Model GR), with a ±20,000 pound full scale capacity, and ac signal conditioning. The output amplifier was capable of producing full scale recorder pen motion for ranges as low as 500 pounds at rated accuracy of $\pm\frac{1}{4}$ percent.

The plate tests were performed using the apparatus described previously. Alignment of the specimen and fixture was accomplished by replacing the flat-faced loading rod (see Fig. 5) with a sharp-pointed conical alignment rod. The moving crossbeam was lowered until the rod point indented the lower crossbeam of the machine, marking the center of the load axis. The support fixture was aligned to this center and held in place by two steel pins. The three LVDT's were then positioned and held by double-coated masking tape to the lower crossbeam.

The LVDT's were calibrated at this point by screwing a thick circular flat plate onto the end of the alignment rod. This calibration plate was small enough in diameter to fit within the 5.22-inch support plate opening. While moving the crosshead downward by known amounts of displacement, the signal balancing unit and strip chart recorder amplifiers were adjusted to effect the calibration.

The plate specimen was then installed and the strain gauge leads connected. Each plate had a small center punch mark on its top face, which was used to align the plate by matching that mark with the point of the alignment rod. The plate was then held in position by three sets of bolts and washers around its edge. The load cell circuit was zeroed and calibrated (500 pound internally simulated load), and the strain gauge and LVDT circuits were checked and zeroed. The strain gauge scanner unit was set to scan through all the gauges in sequence and repeat continuously, at the nominal rate of 0.2 sec per gauge. The conical alignment rod was removed from the load cell and replaced by the flat-faced loading rod. The crosshead was lowered to bring the loading rod in contact with the plate surface, a five-pound preload was applied to hold the plate secure, and then the holddown bolts and washers were removed.

The crosshead motion, the strain gauge scanner/recorder, the LVDT strip chart recorder, and the load cell chart recorder were started simultaneously. From that moment until the end of the test, the operation was automatic and monitored continuously. The displacements, strains, and load values were all related by the time parameter, since the various chart speeds and strain gauge scanner speed were all accurately measured in advance.

Material Properties Tests

Eight tension coupons and four compression rods were tested for both the $\frac{1}{4}$- and $\frac{1}{8}$-inch plate material. The tension coupon tests were also performed in the Instron machine (Fig. 4), in the upper part above the moving crossbeam. The load cell was attached through the upper crossbeam, with a universal-joint coupling into an upper grip, which held the upper end of the tension coupon. These items are not shown here. The coupon was held from below by a lower grip, shown in Fig. 4, rigidly attached to the moving crossbeam. The tension was applied by the downward moving crossbeam. The load was measured using the Instron load cell, while the strain was measured by both the strain gauges and a clip-on extensometer.

The strain gauges were from the same lot as those used on the plates, with gauges bonded to opposite faces of the tension coupons. A typical tension coupon with gauges installed is shown in Fig. 9. These strain gauges were applied using the same techniques and materials described previously for the gauges on the plate specimens. For each plate thickness, the four coupons numbered 1, 2, 8, and 9 had the dual-element gauges while the four numbered 3, 6, 11, and 12 had the single-element gauges.

The extensometer (Instron Model G-51-11) was a strain-gauge element type that contacted one face of the coupons with dual knife edges held by spring clips. This unit had a one-inch nominal gauge length, a maximum extension of 0.1 inch, and an accuracy of $\pm\frac{1}{4}$ percent (manufacturer's calibration data). The extensometer signal was recorded through an amplifier as chart drive motion on the Instron recorder. The extensometer was used to check out the accuracy of the strain gauges in the high strain ranges (1 to 10 percent), for all eight of the $\frac{1}{8}$-inch thick coupons and for two (one with single-element and one with dual-element strain gauges)

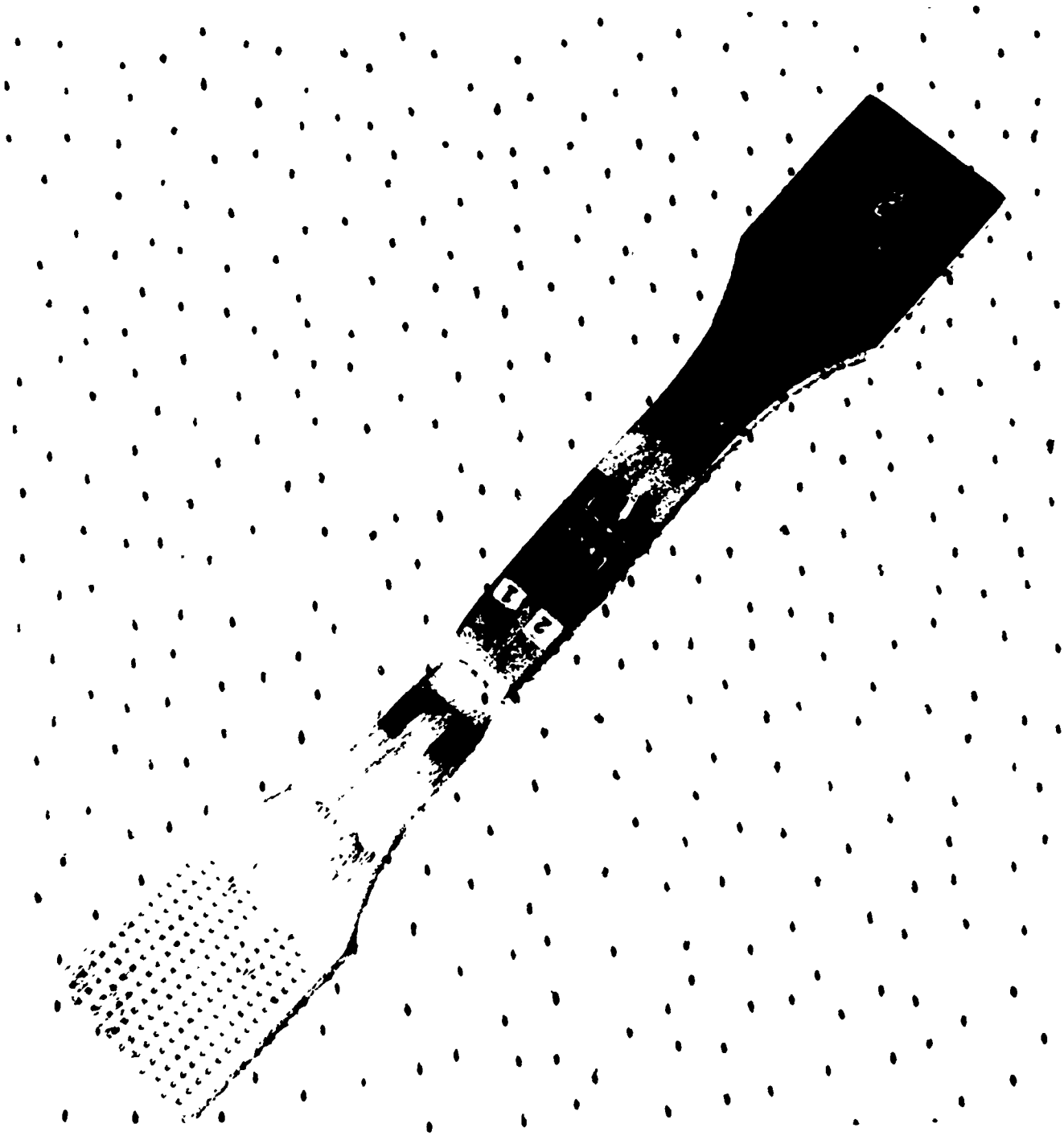

Fig. 9. Typical Tension Coupon

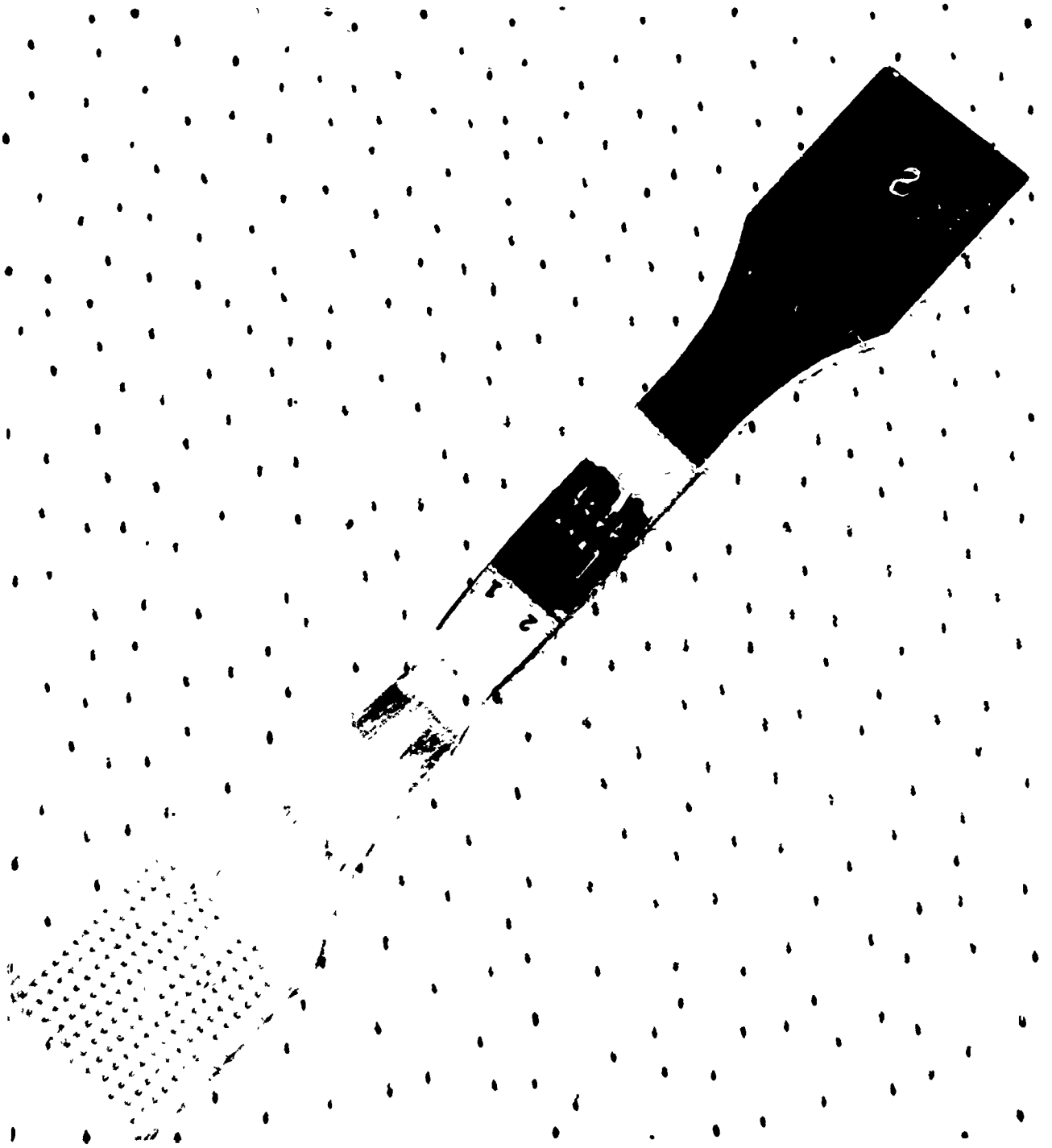

Fig. 9. Typical Tension Coupon

of the $\frac{1}{4}$-inch thick coupons. The net strain gauge error, after data processing, is discussed in Appendix B.

The tension coupons were tested to about 10 percent strain in the Instron testing machine with a universal-joint upper grip and a fixed lower grip. The crosshead speed was set at values that varied among the tests from 0.002 to 0.020 inch per minute. For the tension coupons used here, the nominal strain rate in the gauge section was estimated to be in the range of 600 to 6000 microstrain (10^{-6} inches/inch) per minute.

The load and extension were recorded simultaneously on the Instron chart recorder, with the load cell driving the pen motion, and the extensometer driving the chart motion, producing x-y type records. The strain gauges on the tension coupons were sampled by scanning through the set of gauges at different levels of indicated load. The strain gauge scanner-recorder unit was set to scan once through the set of 2 or 4 gauges, at the rate of 0.1 sec per gauge, therefore taking 0.2 and 0.4 sec for each scan. The corresponding maximum changes in strain during a scan were estimated to be 20 and 40 microstrain.

The strain gauge data were processed by mathematically compensating for the known errors due to transverse sensitivity and bridge nonlinearity, as described in Appendix B.

For the compression tests, the load cell was attached to the lower crossbeam, with a hardened steel compression plate on the load cell upper end. Another compression plate was attached to the underside of the moving crosshead. The compression coupons were placed on the load cell plate and were compressed by the downward moving crosshead plate at a constant speed of 0.002 inch per minute. This produced a strain rate of 2000 microstrain per minute on the

one-inch long rod specimens. These tests were stopped at about 2 percent strain because calculations and exploratory tests indicated a tendency for plastic buckling at higher strains.

The Instron recorder was operated in a strip chart mode, with the load plotting across as the chart moved down at a known constant speed. The compression was recorded indirectly by relating the chart motion to the crosshead motion and adjusting for the calibrated deformations of the machine.

3. DATA

Material Properties

The tension and compression coupon tests provided data to determine the true stress-strain curves for the plate material. The corrected strain gauge data were used for this purpose, and the details of the strain gauge data processing are given in Appendix B.

A typical load versus extension record is shown in Fig. 10, which indicates that the material had a nonsmooth tension stress-strain curve at high plastic strains. This was most probably due to a nonuniform distribution of yielding known as the Portevin-le Chatelier effect (Ref. 20 and, for a more recent example, Ref. 21), in which incremental plastic strains are confined to concentrated yield bands, similar to Lüders bands in steel. A smooth average curve could be faired through this trace, with little difficulty. The digitalized strain gauge data, however, were recorded at nonuniform discrete intervals, which appeared to add a certain amount of random scatter, but it was still possible for an accurate curve to be faired through the digital data, as shown in Fig. 11.

In this way, stress-strain curves were constructed for each tension coupon, and from these, true stress versus average strain curves were calculated by averaging the individual values of corrected strain gauge data at intervals of true stress. The method of calculating true stresses is given in Appendix C. These curves are shown in Figs. 12 and 13 for the $\frac{1}{8}$- and $\frac{1}{4}$-inch plates, and an analysis of the variations in the coupon data are given in Tables 2 and 3. The tables indicate that the plate material was essentially isotropic and homogeneous, since the differences between the tension properties in the longitudinal and transverse

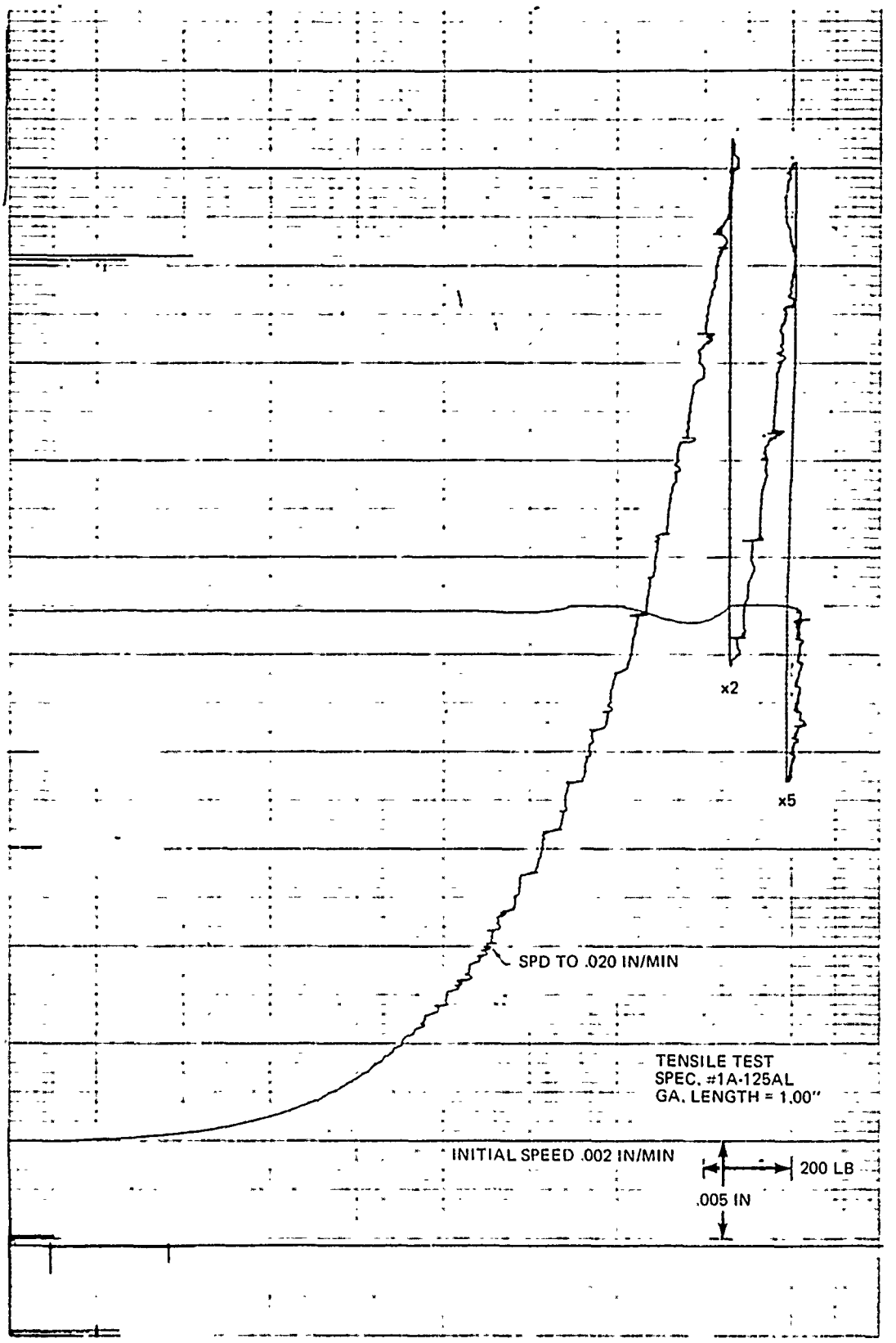

Fig. 10. Typical Load-Extension Record

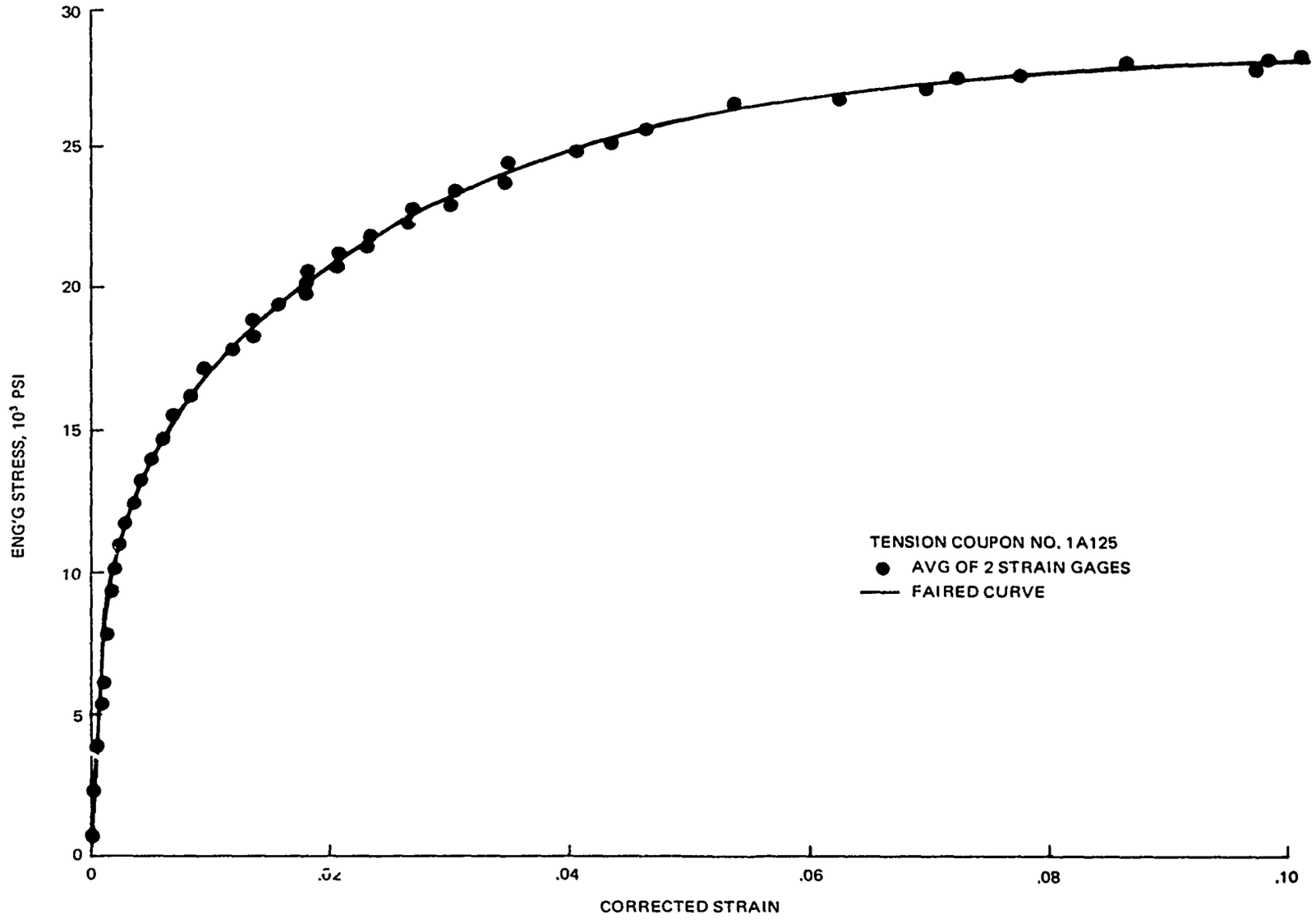

Fig. 11. Typical Strain Gauge Data

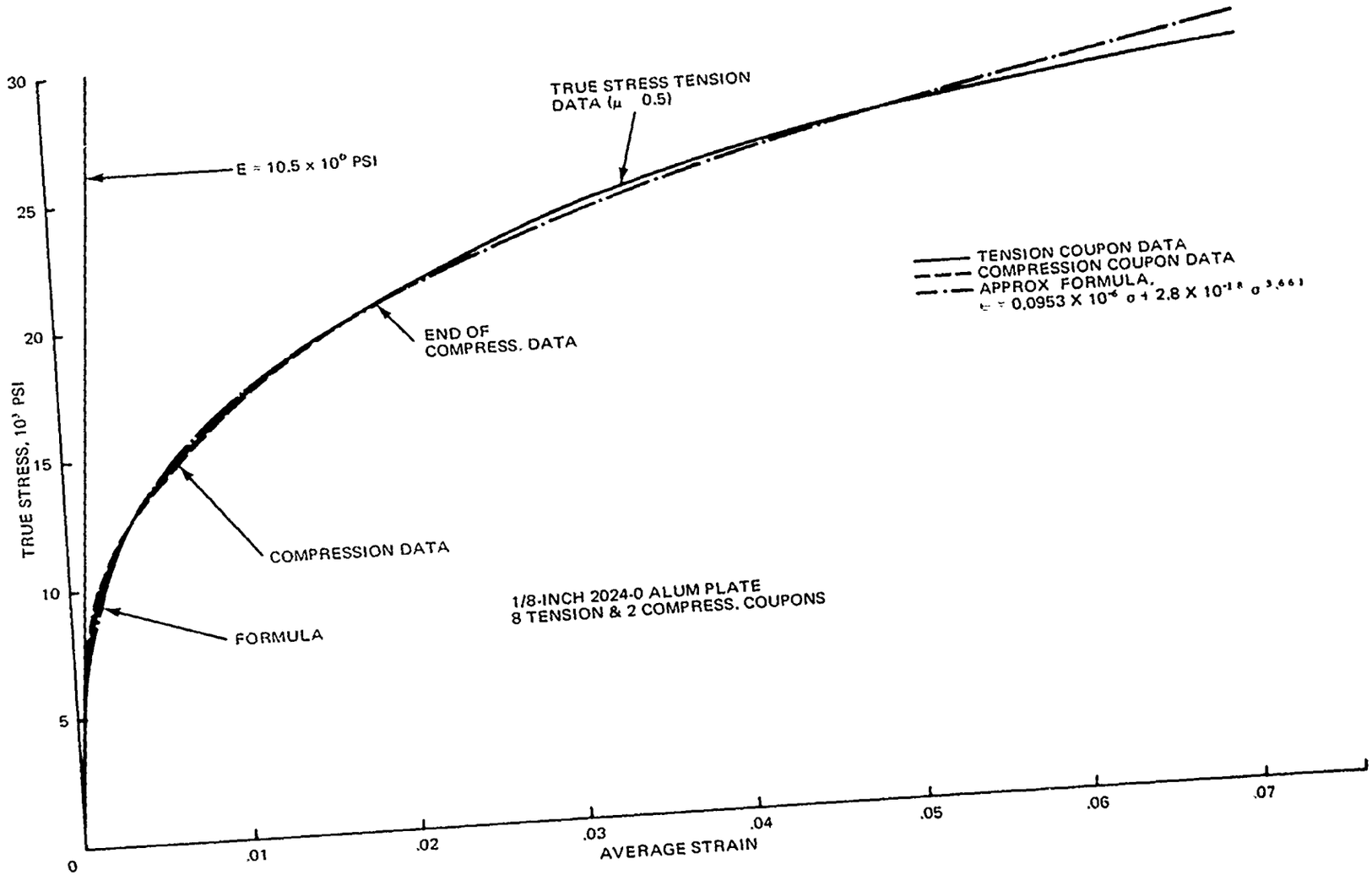

Fig. 12. Average Stress-Strain Curve for 1/8-Inch Plate Material

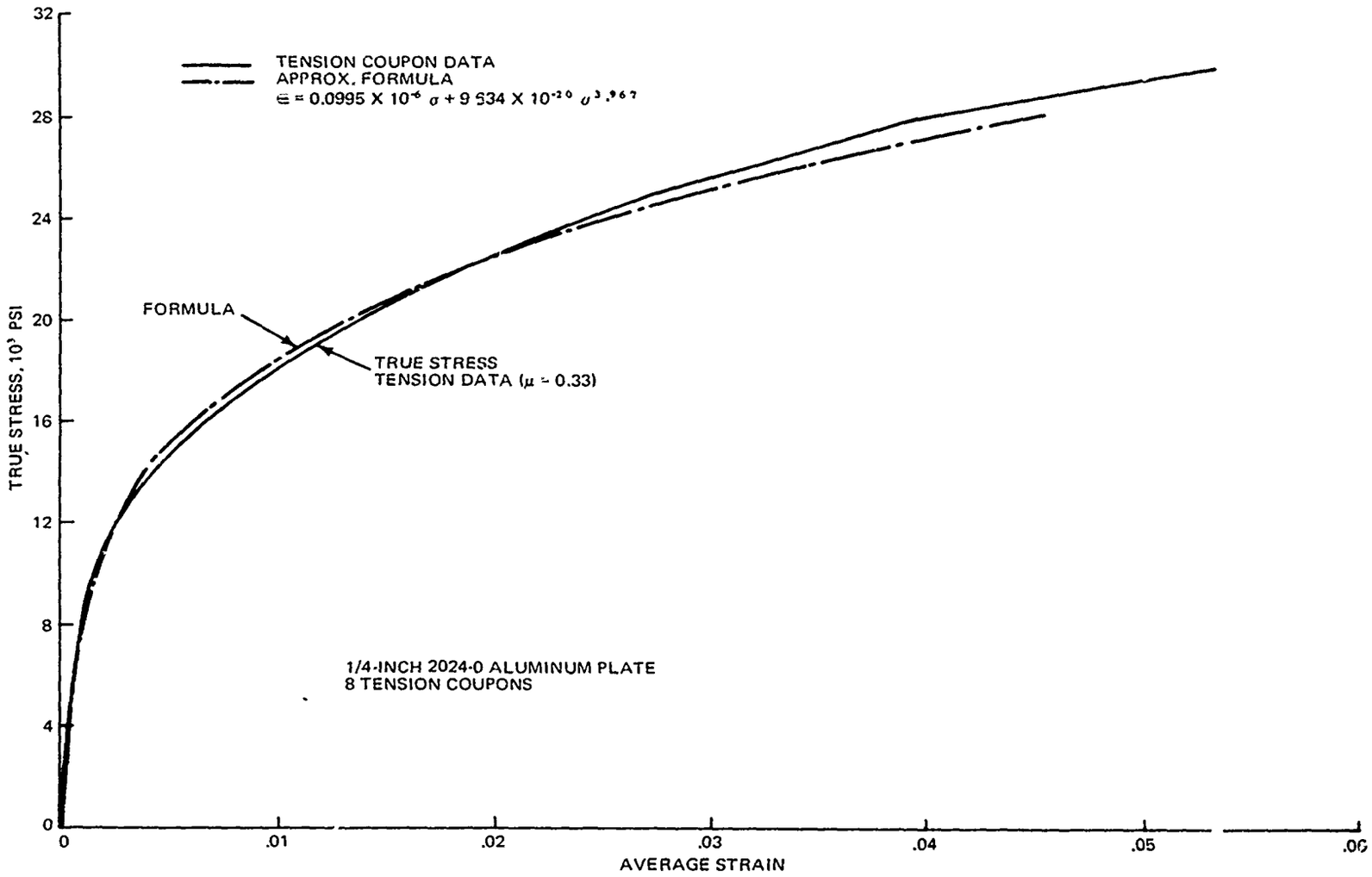

Fig. 13. Average Stress-Strain Curve for 1/4-Inch Plate Material

TABLE 2 SUMMARY OF COUPON TESTS - [illegible]-INCH PLATE

a. Tension Data

Coupon No.[a]	Orientation[b]	E 10^6 psi	Deviation from Avg[c] %	True σ ϵ = 0.5% ksi	Deviation from Avg[c] %	True σ ϵ = 2% ksi	Deviation from Avg[c] %	True σ ϵ = 5% ksi	Deviation from Avg[c] %
1	T	10.3	+ 2	13.80	+ 3.6	21.3	+ 2.3	27.2	+ 0.7
2	L	9.97	- 5	13.40	+ 0.8	20.9	+ 0.5	27.3	+ 1.1
3	T	10.0	- 5	13.40	+ 0.8	21.0	+ 0.9	26.8	- 0.8
6	L	10.0	- 5	13.30	0	20.6	- 1.0	27.2	+ 0.7
8	L	11.4	+ 9	13.05	- 1.9	20.4	- 2.0	26.9	- 0.4
9	T	11.9	+ 13	13.40	+ 0.8	–	–	–	–
11	T	10.2	- 3	13.10	- 1.5	20.6	- 1.0	26.9	- 0.4
12	L	10.2	- 3	13.00	- 2.3	20.9	+ 0.5	26.8	- 0.8
Avg of	L	10.4	- 0.9	13.20	- 0.7	20.7	- 0.5	27.0	+ 0.1
Avg of	T	10.6	+ 0.9	13.40	+ 0.7	20.9	+ 0.7	26.9	- 0.1
Avg of	All	10.5	± 5.6[d]	13.30	± 1.5[d]	20.8	± 1.2[d]	27.0	± 0.7[d]

b. Compression Data

1		10.70	+ 1.4	13.40	0	20.7	–	–	–
2		10.39	- 1.5	13.40	0	–	–	–	–
Average		10.55	± 1.5	13.40	0	20.7	–	–	–

a. Locations shown in Fig. 1

b. Longitudinal or transverse to mill rolling direction

c. With respect to over-all avg, last no. in preceding column

d. Average deviation from over-all average

TABLE 3 SUMMARY OF COUPON TESTS - $\frac{1}{8}$-INCH PLATE

Coupon No.[a]	Orientation[b]	E 10^6 psi	Deviation from Avg[c] %	True σ @ ϵ = 0.5% ksi	Deviation from Avg[c] %	True σ @ ϵ = 2% ksi	Deviation from Avg[c] %	True σ @ ϵ = 5% ksi	Deviation from Avg %
1	T	10.21	+ 1.6	14.8	+ 0.7	22.3	- 1.8	29.0	+ 1.7
2	L	9.60	- 4.5	15.0	+ 2.0	23.2	+ 2.2	30.3	+ 2.7
3	T	10.20	+ 1.5	14.7	0	22.5	- 0.9	28.9	- 2.0
6	L	10.70	+ 6.5	14.6	- 0.7	22.8	+ 0.4	29.9	+ 1.4
8	L	9.40	- 6.5	14.6	- 0.7	22.9	+ 0.9	30.0	+ 1.7
9	T	9.70	- 3.5	14.5	- 1.4	22.4	- 1.3	28.8	- 2.4
11	T	10.15	+ 1.0	14.5	- 1.4	22.2	- 2.2	28.6	- 3.1
12	L	10.45	+ 4.0	14.8	+ 0.7	23.1	+ 1.8	30.6	+ 3.7
Avg of L		10.04	- 0.1	14.8	+ 0.7	23.0	+ 1.3	30.2	+ 2.4
Avg of T		10.07	+ 0.1	14.6	- 0.7	22.4	- 1.3	28.8	- 2.4
Avg of All		10.05	± 3.6[d]	14.7	± 1.0[d]	22.7	± 2.3[d]	29.5	± 2.3[d]

a. Locations in Fig. 1

b. Longitudinal or transverse to mill rolling direction

c. With respect to over-all avg, last no. in preceding column

d Average deviation from over-all average

directions were small and the deviations of individual coupons from the average were generally also small. One exception was the elastic moduli. These measurements were made more difficult by the small elastic strain limit of the material, so that the variability was probably caused more by instrumentation and data interpretation errors than by any actual variation in the moduli.

Note that only 2 compression tests are reported, both for the $\frac{1}{8}$-inch plate. Data from the other compression tests were judged to be invalid because the elastic slopes of those stress-strain curves did not agree sufficiently with the known elastic modulus for this material. Those specimens were too stiff for satisfactory use in the testing machine. The specimen length had to be kept short to prevent plastic buckling, but this caused the specimen stiffness to exceed the machine stiffness. Large errors in the calculated specimen strains resulted, because of apparently uncontrollable variations in machine stiffness from test-to-test. This problem could have been avoided by repeating the tests with a one-inch gauge length compressometer to directly measure the deformations on the specimens. It was decided to abandon further compression tests, however, since the two acceptable tests confirmed the published information that the compression and tension stress-strain curves were nearly identical, as shown in Fig. 12.

A mathematical representation of the stress-strain curves of the type

$$\epsilon = (\sigma/E) + \alpha\sigma^n \tag{1}$$

was required for use in the theoretical prediction of the plate behavior, and therefore such curves were fitted through the test data. The first term on the right hand side of Eq. (1) is the elastic strain and the second the plastic strain. The approximating curves plotted in Figs. 12 and 13 represented the best

compromises to fit over the whole range of strains. Apparently, the plastic strains did not fit the second term of Eq. (1) very well over the range. A least squares curve-fitting analysis showed that a slightly better fit would result with a formula using $\alpha e^{n\sigma}$ for the plastic strain term. However, theoretical analysis requires that the stress-strain law be in the form of Eq. (1).

A better theoretical approach would be to approximate the stress-strain curve by piecewise linear segments. This would allow the representation to be as accurate as desired, by varying the number of points connected by the straightline segments.

Plate Behavior

Test data from the three plates are discussed in this section. For each plate, a basic set of data includes:

- Data histories - deflections and strains plotted versus load, at regular intervals up to the maximum test load
- Strain distributions - strains on lower (tension) surface plotted versus radial position at several load levels
- Symmetry check - radial strains from three gauges equally spaced around a 1.0-inch radius circle, on upper and lower surfaces, plotted versus load.

Also to be discussed are the corresponding theoretical predictions of the Grumman finite element computer code AXSHEL (Axisymmetric Shell Analysis) of the PLANS (Plastic and Large deflection Analysis of Structures System). The version of AXSHEL used here is capable of treating the combined nonlinearities associated

with elastic-plastic material behavior, and large deformations for bending and membrane behavior. It does not include transverse shear stiffness nor local (three dimensional) stress distributions at the loaded areas. A very brief description of the general theoretical method, and the specific finite element idealizations used here is given in Appendix D. A more complete description can be found in Refs. 22, 23, and 24.

Data for the $\frac{1}{8}$-inch thick plate No. 1A125, having a supported diameter-to-thickness ratio of $D/h \approx 40.6$ is given first, in Figs. 14 through 19. This plate was tested to a maximum load of 1140 pounds, developing a peak deflection of approximately 2.6 times the thickness. Two finite element theory models were used, one having 14 and the other 27 annular plate elements (Fig. D-1). load increments of 2.0 pounds were applied to both models.

The loading was modeled by assuming a uniform contact pressure between the load rod and plate. It is known that the contact pressure between a rigid rod and an elastic surface is highly nonuniform with more contact pressure at the edge than at the center of the rod. However, it was decided to try to use the uniform contact pressure as a simple first approximation to the more complex actual distribution, since the loaded area was small compared to the whole plate; only the region near the load was expected to be affected.

The deflection data for this plate are shown in Fig. 14. The main feature to note is the distinctly nonlinear behavior, with plasticity at first causing reduced stiffness, followed by a restiffening of the plate at higher loads as large deflections ($w_o/h > 1$) are developed. The measured motion of the load rod, in contact with the upper surface, is plotted in Fig. 14 as the

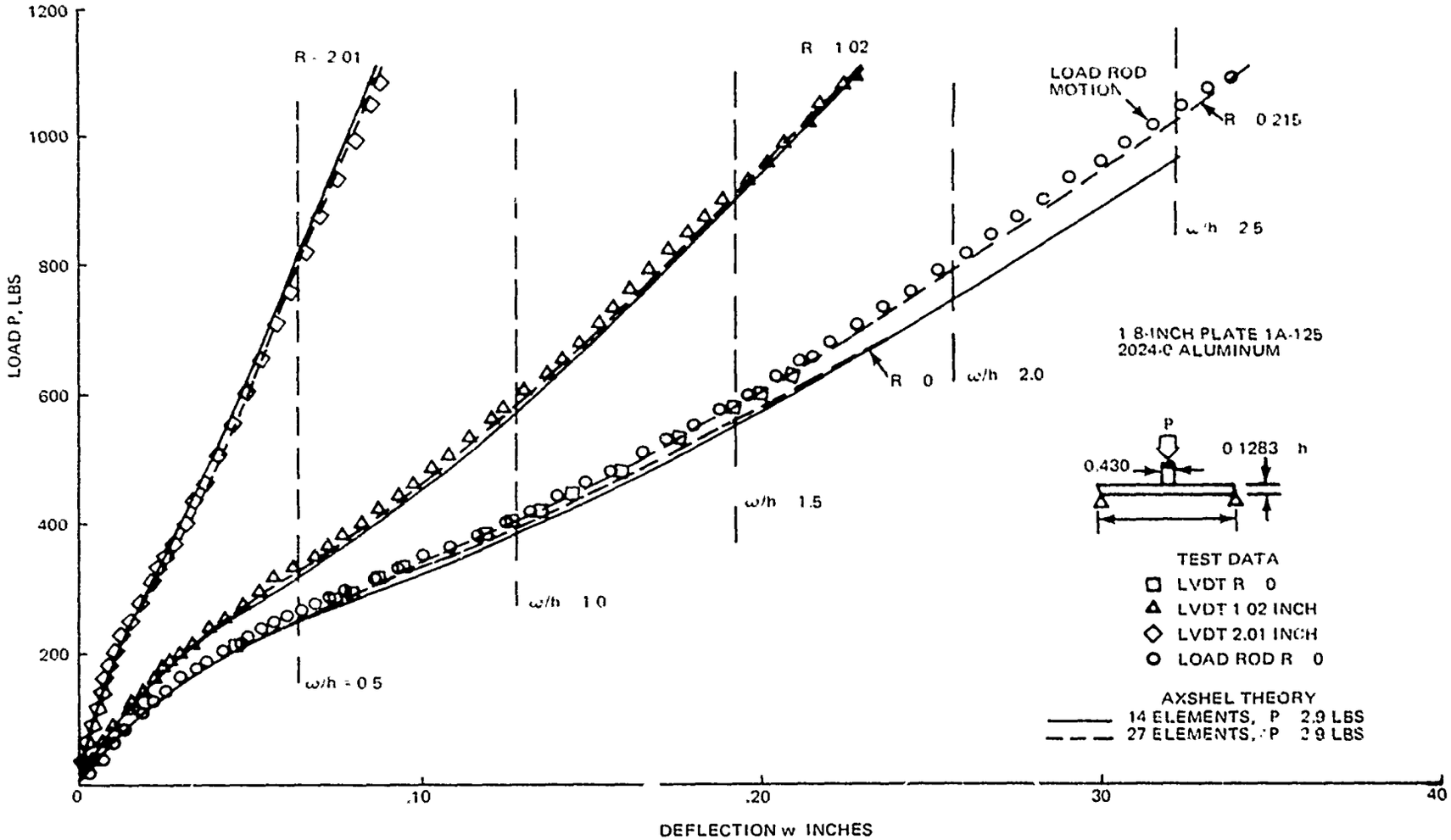

Fig. 14. Deflection History, Plate 1A125

circular data points. The square data points show the data from the central LVDT, which was in contact with the lower surface at the center. That LVDT had a useful range at about 0.22 inch, so only the load rod data are available after that point.

The predicted displacements curves are drawn for the location R = 0.215 inch, under the edge of the loading rod, as well as for the locations of the three LVDT transducers. The predictions agree very well with the data for the two outer positions. However, both the load rod motion and the central LVDT data correlate more closely with the prediction for the motion of the load rod edge at R = 0.215 inch, than with the predicted central deflection at R = 0. It could be expected that the load rod would tend to contact the plate at its edge circle as the deformation progressed and the data seem to confirm that. However, the measured central deflection being nearly equal to the rod edge deflection indicates that the plate remained nearly flat under the load rod (at least up to 0.22 inch deflection).

This difference between the measured and predicted central deflections was probably caused by inaccuracy of the assumed contact pressure distribution. Away from the rod edge, the plate behavior cannot depend significantly upon the load distribution, but only upon the total load level.

Figure 14 shows that nearly doubling the number of elements in the theoretical model, from 14 to 27, produced a small increase in predictive accuracy for deflections, resulting in excellent correlation with the test data, but the computing cost was nearly doubled. Probably, less than 14 elements would have been sufficient to predict the deformations, if an error of, say, five percent would have been tolerable.

The processed strain gauge data, as a function of applied load, are shown in Figs. 15 and 16. The lower (tension) surface data are replotted in Figs. 17 and 18, as strain distributions along a radius, for several representative load levels. The upper surface circumferential gauge and both radial gauges at $R = 0.51$ inch failed after 300 pounds load, perhaps because they were too close to the loading rod. There was no strain gauge at $R = 0$ on the top surface, but the theoretical curve is given for that location for reference purposes.

The most noticeable features of the strain data are that the circumferential strains were greatly dominant over most of the plate, while the radial strain component drops rapidly with radius, being significantly large only in the region under the load circle. Apparently, the flow mechanism is primarily circumferential, but a radial "plastic hinge" effect is important near the plate center. This is qualitatively consistent with previously reported results for mild steel simply supported circular plates (Refs. 5 and 14).

The correlation between measured and predicted strains is good only on the outer half of the plate away from the load rod, where the strains are relatively low. The theory greatly overpredicted the tension strain near the plate center, with the error increasing with greater load levels. At the load level of 1017 pounds the predicted strain at the center was almost twice the measured value (Fig. 17). The predictive accuracy improved with radius, as the strain level dropped. In general, the overprediction increased with increasing strain.

This large error in strain predictions at the plate center was most likely caused by the assumed distribution of contact pressure, as previously described. Since the strain is usually more

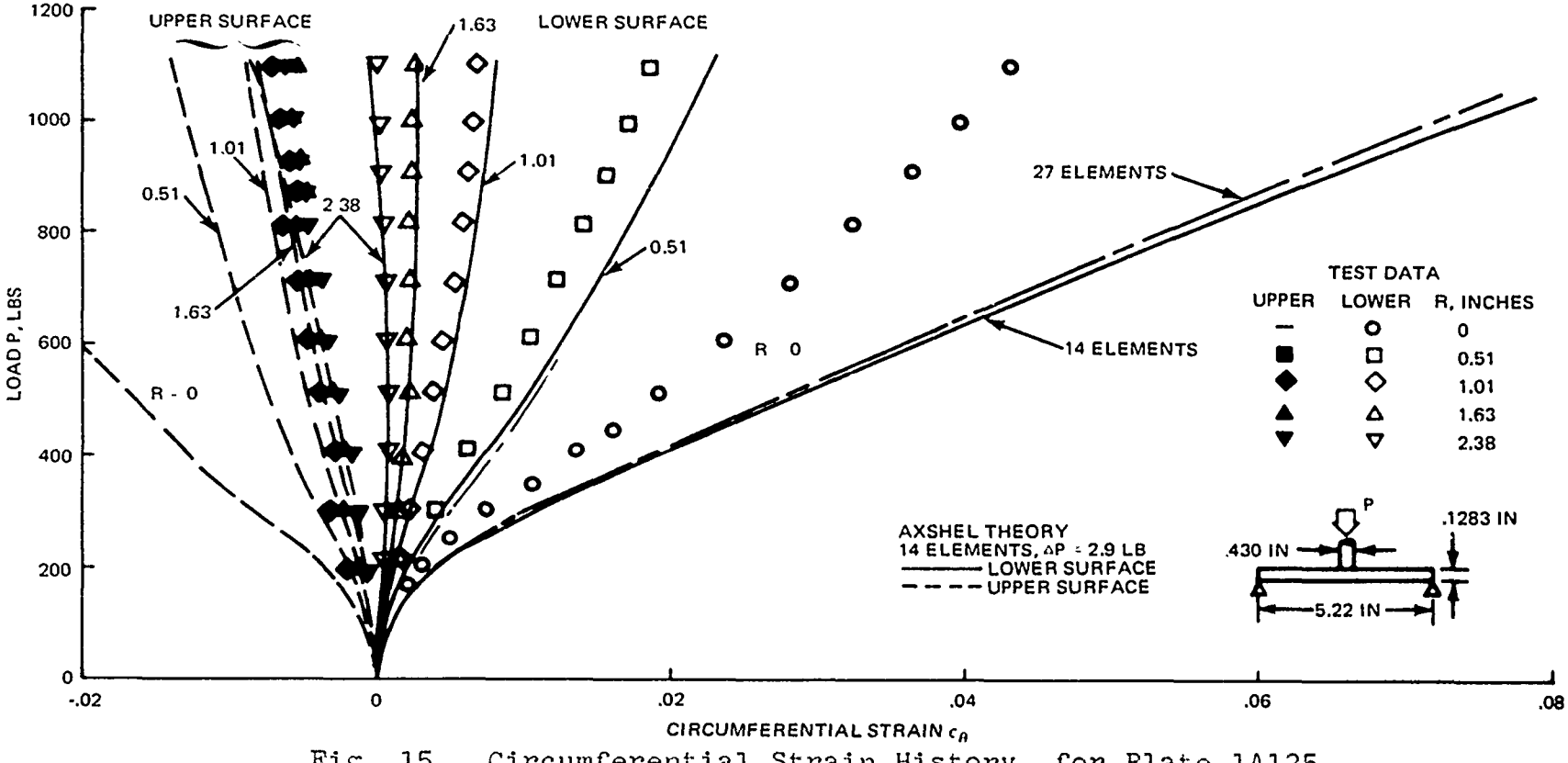

Fig. 15. Circumferential Strain History, for Plate 1A125

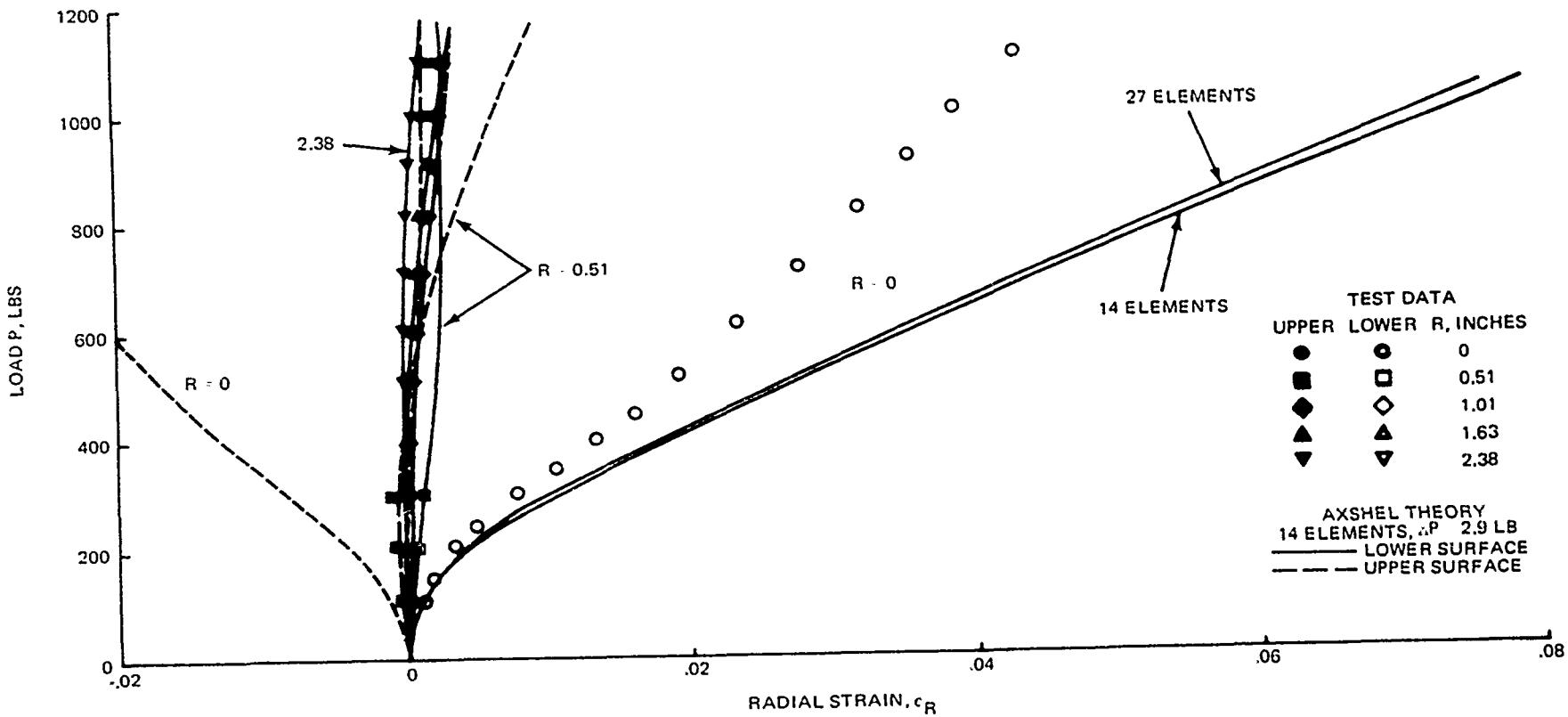

Fig. 16. Radial Strain History, Plate 1A125

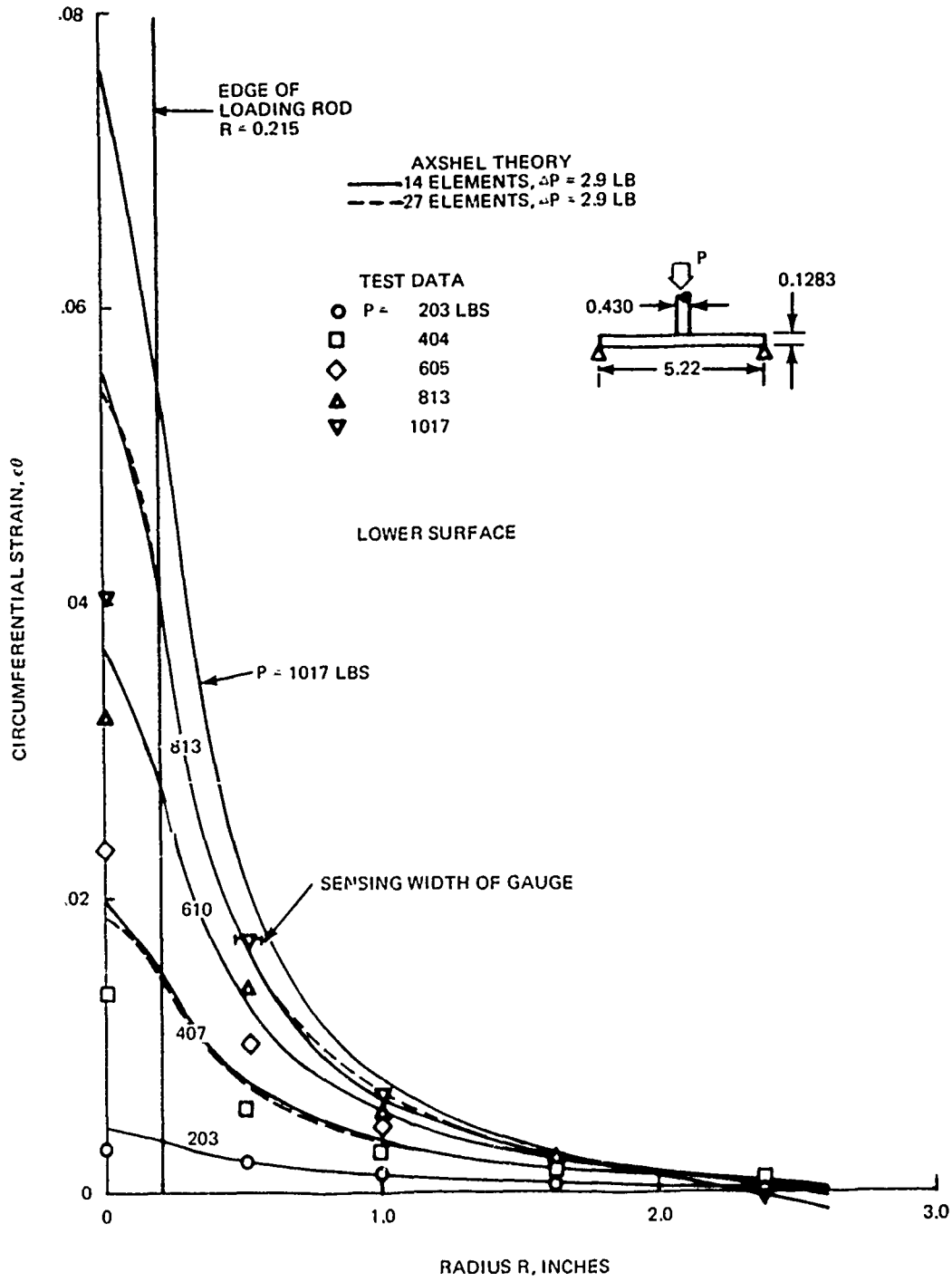

Fig. 17. Circumferential Strain Distribution, Lower Surface, Plate 1A125

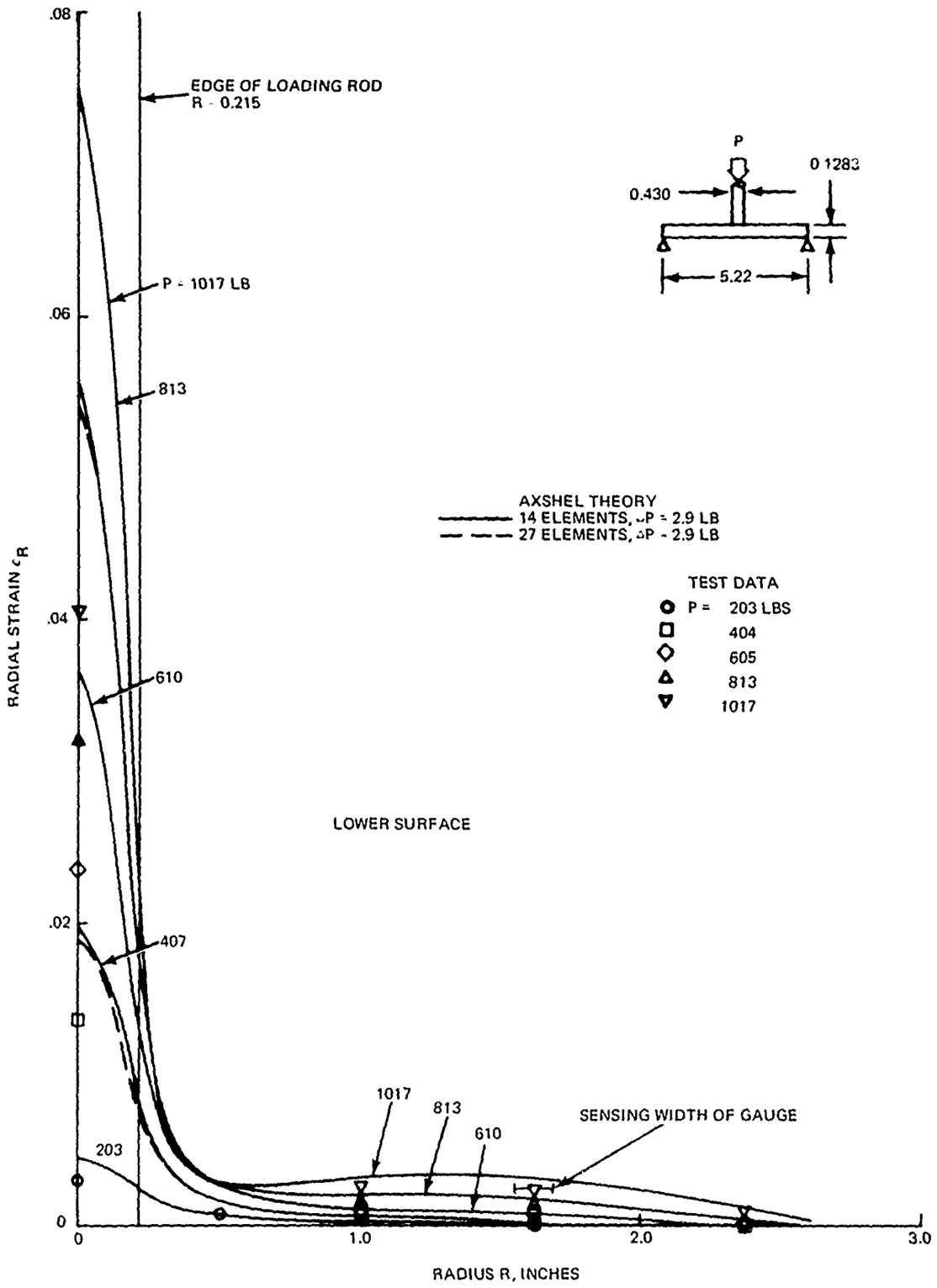

Fig. 18. Radial Strain Distribution, Lower Surface, Plate 1A125

sensitive to local conditions, it is to be expected that the strain predictions under the load would be more in error than the deflections.

Another possible cause for the strain prediction error might be that the theory does not include the effects of transverse shear or of local contact stresses. Since the latter will be generally compressive in the region of the plate under the loading rod, it is to be expected that the measured tensile strains will be reduced at the plate center. Timoshenko (Ref. 25) discusses this case for purely elastic behavior, but provides a formula for the peak tension strain only for the limiting case of a uniformly loaded circle of very small size compared to the thickness. Since the case at hand has a loaded circle diameter $2c = 0.415$ inch and a thickness $h = 0.128$ inch, the ratio $2c/h = 3.24$ is outside the range of applicability of Timoshenko's formula. Anderson and Shield (Ref. 26) examined the problem using perfect plasticity and the Tresca yield condition. They found that the local behavior under the load governed the plastic collapse load for $2c/h < 1$, while plate theory was sufficiently accurate to predict the collapse load for $2c/h > 3$. The three plates tested here have values of $1.4 < 2c/h < 3.2$ (listed in Table 4), that are in the range where the contact stresses can be expected to have an effect on the over-all plate behavior; for example, on the deflections.

The strain predictions using a 27-element theoretical model (Appendix D) are plotted for two load levels, as the dashed curves, Figs. 17 and 18. As with the deflections, they show very little difference from the 14-element model and a still fewer number of elements would have been sufficient.

At the plate center, the radial and circumferential strains are identical, as required by the symmetry, so that a single strain

Table 4 LOAD CONCENTRATION PARAMETER

	Plate Specimen		
	1A125	4A125	4A250
2c	0.415	0.375	0.375
h	0.1283	0.1286	0.2615
2c/h	3.2	2.9	1.4

gauge was used for both strain components at that location. The actual symmetry of the plate test was checked by comparing the strain data from the radial gauges installed along a 2-inch diameter circle at 120 degree intervals. These strain data are shown in Fig. 19. Evidently the symmetry on the bottom surface shows some variance among the three gauges. This leads to a degree of uncertainty about the accuracy of the test data for this plate, because the variation is on the surface having the largest strains.

Plate test 4A125 was essentially a duplicate of the first test, except that the load rod diameter was reduced to 0.375 inch to increase the distance between the rod edge and the innermost strain gauges, in hopes of preventing any premature gauge failures.

The test data and predictions of the finite element theory are shown in Figs. 20 through 24. Test data for this plate were qualitatively similar to that for the first plate, with slight increases in the central deflection and strains near the load that are attributed to the greater load concentration. Two sets of theoretical predictions were made for this plate. One assumed a

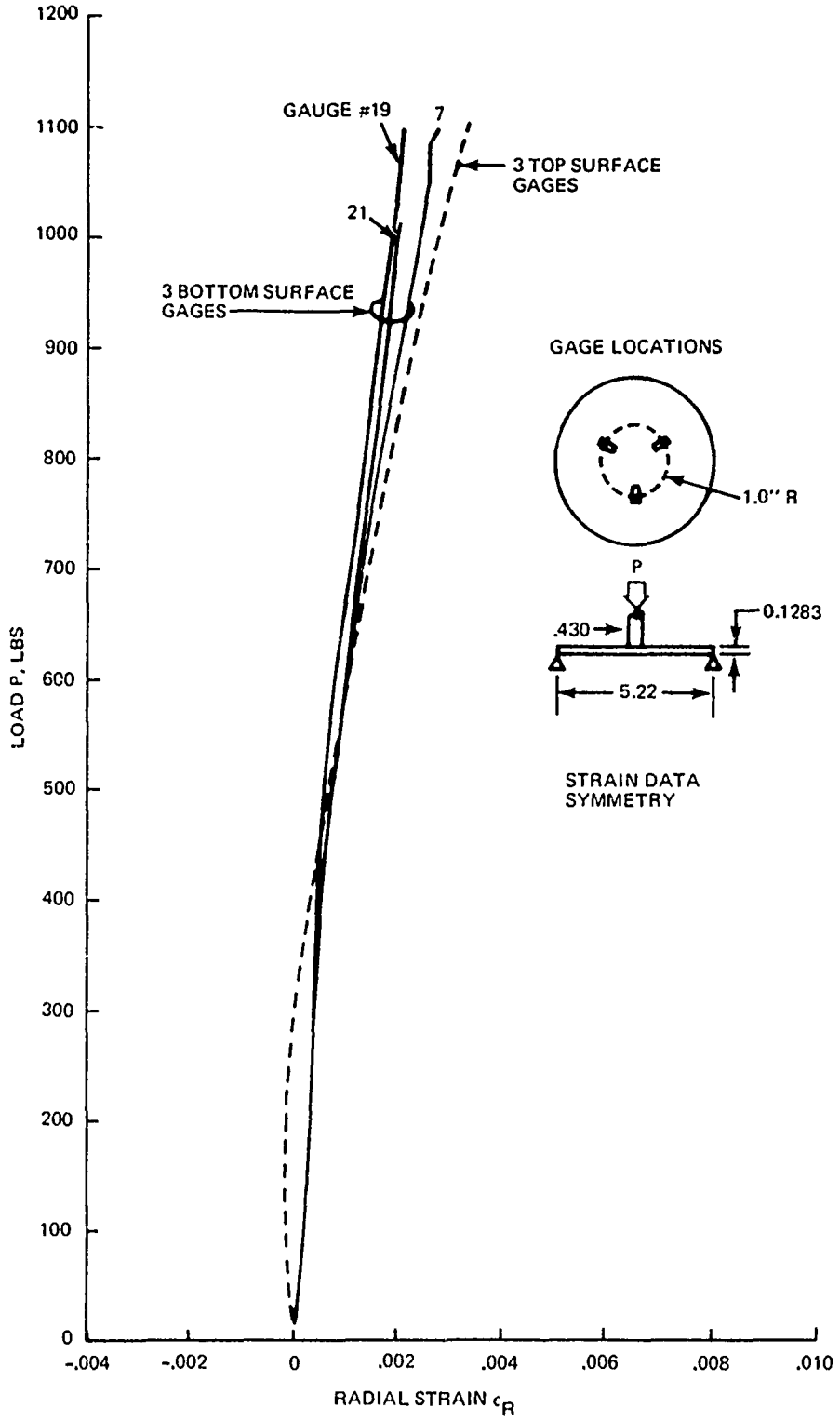

Fig. 19 Symmetry of Strain Data, Plate 1A125

uniformly distributed contact pressure under the loading rod, as before, and the other assumed a line load concentrated along the edge circle of the loading rod. The circular line load case was added because the data from the previous plate indicated that the assumption of uniform contact pressure was inadequate. The actual contact pressure was expected to be somewhere between the two limiting cases of uniform pressure and circular line load.

The load versus deflection data in Fig. 20 show only the measured motion of the load rod, because an electrical circuit failure between the three LVDT displacement transducers and recorder eliminated their records.

Figure 20 shows various types of theoretical predictions for deflection, generated by AXSHEL as it was being developed during this test project. The solid curves are for the predictions that assumed a uniformly distributed contact pressure under the loading rod. At first, the theory contained only the elastic-plastic material behavior with small deflections and strains (the lower curve). But the test data showed that after plasticity began, the plates were stiffer than predicted by that restricted theory. The small deflection plastic bending theory overpredicted the deformations and strains, starting with a central deformation of about 40 percent of the plate thickness ($w_o/h \approx 0.4$). This indicates that the membrane strains and stiffness became significant at that point. The prediction seemed to be approaching a collapse load — a zero-stiffness condition defined as a large deflection increase for a very small load increase — at about 500-600 pounds. The test data, however, showed no collapse trend, but an indication to regain stiffness continually after $w_o/h = 0.7$. This trend was still progressing when the test load was arbitrarily stopped at about $w_o/h = 2.5$.

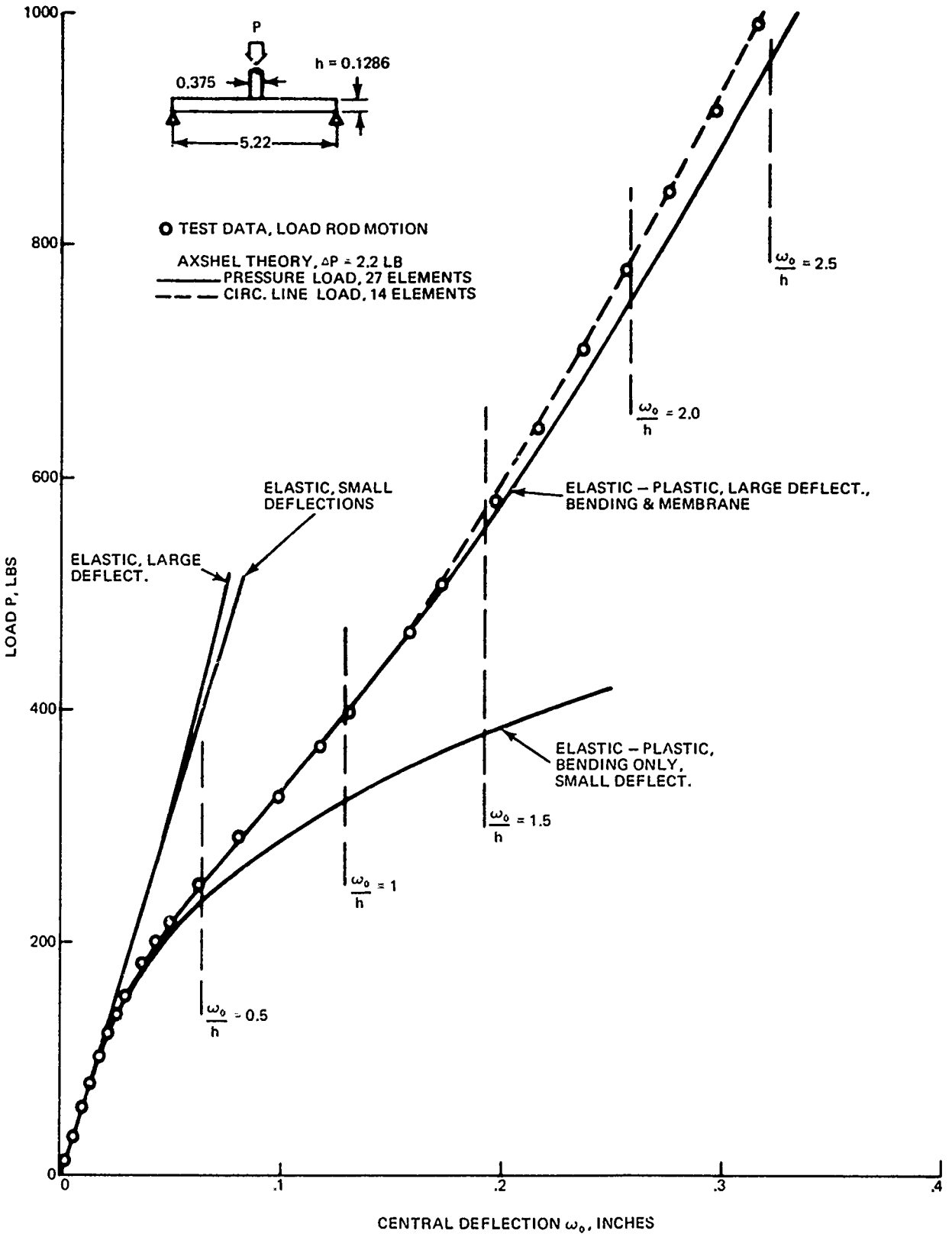

Fig. 20. D flection History, Plate 4A125

The linear elastic (small deformation) case is shown for reference purposes. Diverging from it is the elastic large deflection prediction that incorporates the effect of the membrane stresses, generated from large deformations, on the bending stiffness of the plate. Both of these grossly underpredict the deformations, as expected, because of the neglect of plastic behavior.

Finally, the elastic-plastic large deflection theory is plotted that includes both bending and membrane stiffnesses. The solid curve is for the uniform contact pressure and the dashed curve is for the concentrated line load along the loading rod circle. Up to about 400 pounds, the predictions for the two loadings are the same, with an excellent agreement with the test data. At larger loads the theoretical deflections separate, with the circular line loading case producing an excellent prediction of the test data.

The strain data are shown in Figs. 21, 22, and 23, along with the predictions for the two theoretical loading cases. As expected, the two theoretical results are nearly the same away from the loaded area, but diverge greatly at the center, under the load. The strain data agree fairly well with the theory for the circular line load, except on the upper surface at $R = 0.53$ inch, and on the lower surface at the center, $R = 0$. The measured strains at the center of the lower surface fall between the two theoretical limiting cases, but closer to the prediction for the circular line load. This is taken as a confirmation that the actual contact pressure distribution was somewhat nonuniform with a greater concentration of pressure at the rod edge than at the center. The contact pressure distribution can be expected to change with load, depending on the local yielding of material in the contact region.

Note that the two theoretical loading cases produce significantly divergent strains for $R < 0.5$ inch. This is equivalent to four thicknesses $(R/h < 4)$ or 2.7 times the radius of the loading rod.

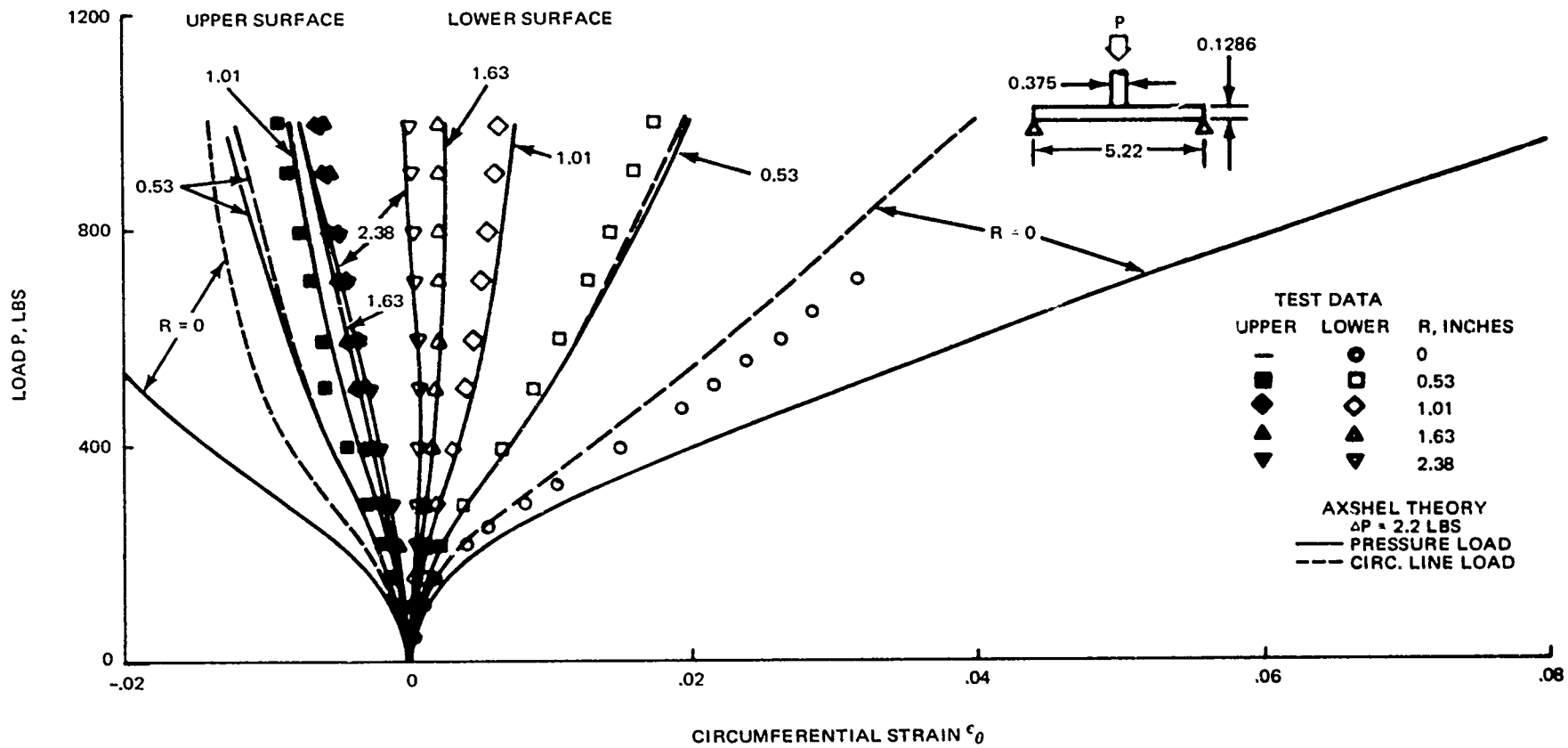

Fig. 21. Circumferential Strain History, Plate 4A125

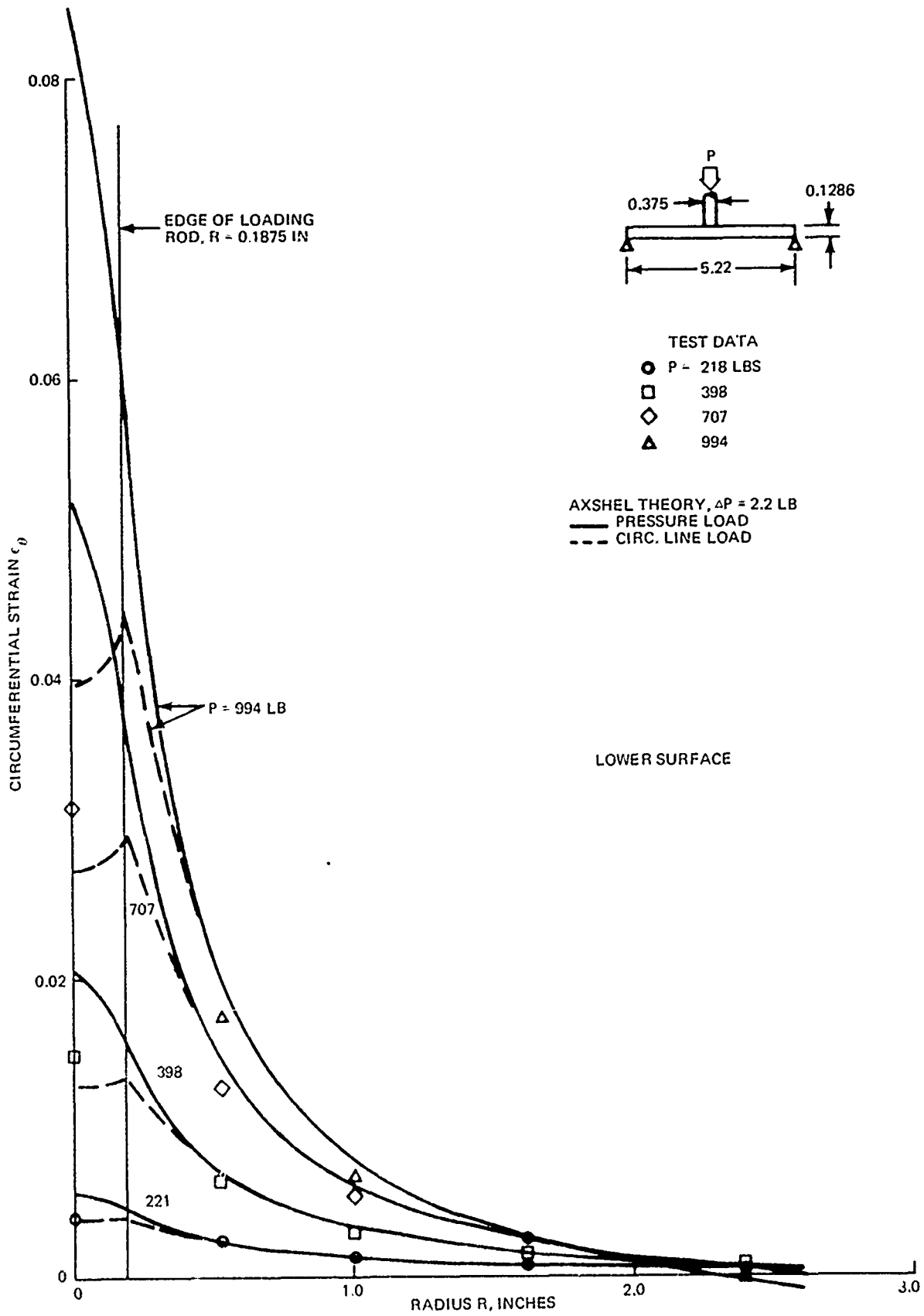

Fig. 22. Circumferential Strain Distributions, Lower Surface, Plate 4A125

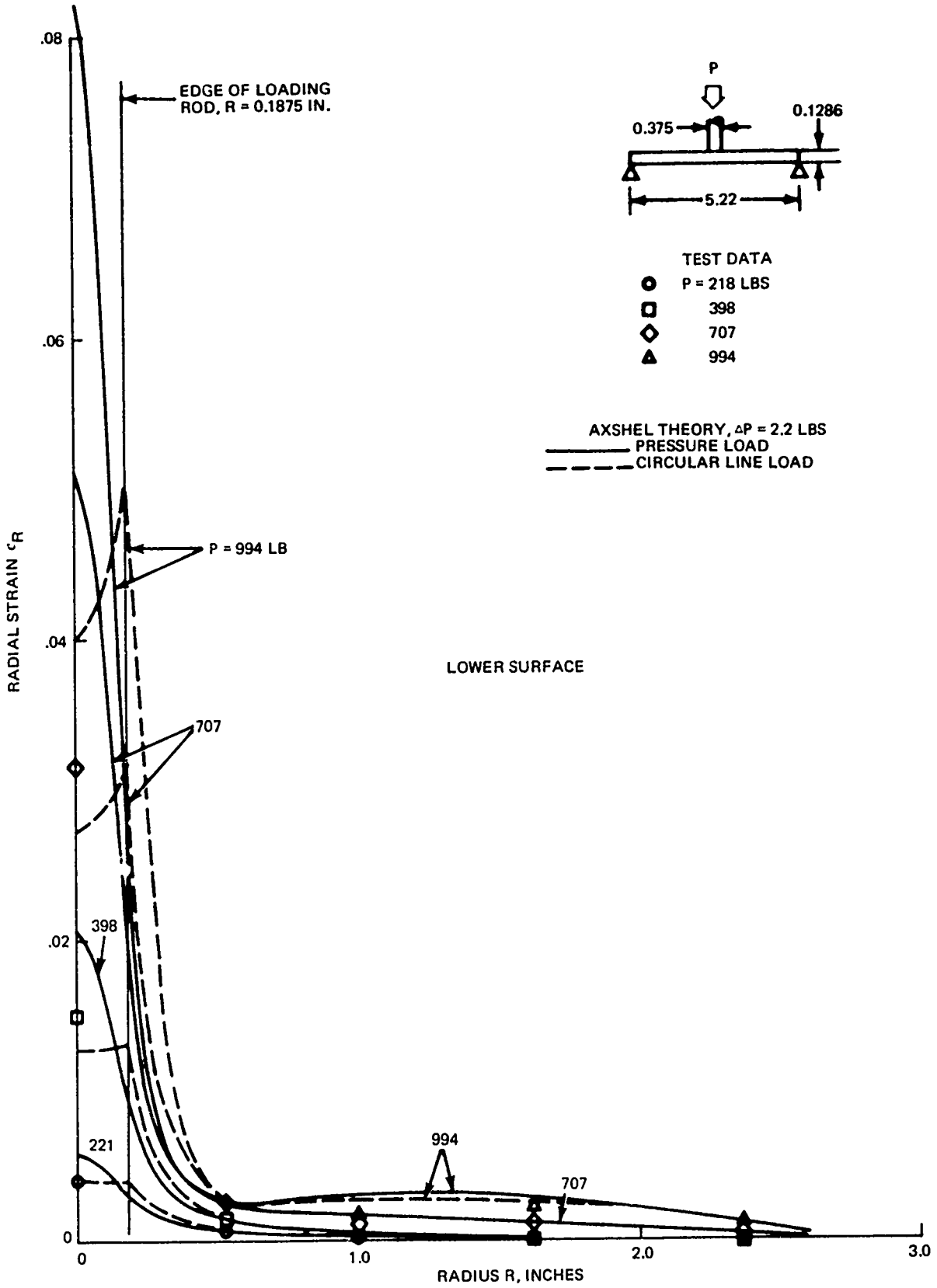

Fig. 23. Radial Strain Distributions, Lower Surface, Plate 4A125AL

Of interest is the symmetry of the strain gauge data in Fig. 24. This time, the strain gauge data indicates a good uniformity around the circumference at $R = 1$ inch, and it can be concluded that the symmetry for this plate was satisfactory.

The strain data for this plate were examined to determine the relative magnitude of the membrane (mid-surface) strains and bending strains. The motivation was to see if the cause of the predictive error could be traced to a particular mechanism, either bending or membrane, so that improvements in the theory could be specifically directed. This was done simply by assuming a linear variation of strain through the thickness of the plate. This is consistent with thin plate theory, in which the thickness contraction due to in-plane strains is not significant. The membrane and bending strains are then

$$\epsilon^M = \tfrac{1}{2}(\epsilon^L + \epsilon^U) \tag{2}$$

$$\epsilon^B = \tfrac{1}{2}(\epsilon^L - \epsilon^U) \tag{3}$$

where the superscripts L and U denote the lower and upper surfaces.

The circumferential membrane and bending strain distributions, calculated from the test data, are plotted in Fig. 25 along with the corresponding theoretical predictions of the AXSHEL code. Note that the predictions are generally more accurate, compared to the test data, for the membrane strains than for the bending strains. This might lead to the judgment that the bending theory was primarily responsible for any lack of agreement between predicted and measured strains. However, the bending strain levels were generally greater than the membrane strain levels, and the predictive error might be caused by a general overprediction of plastic

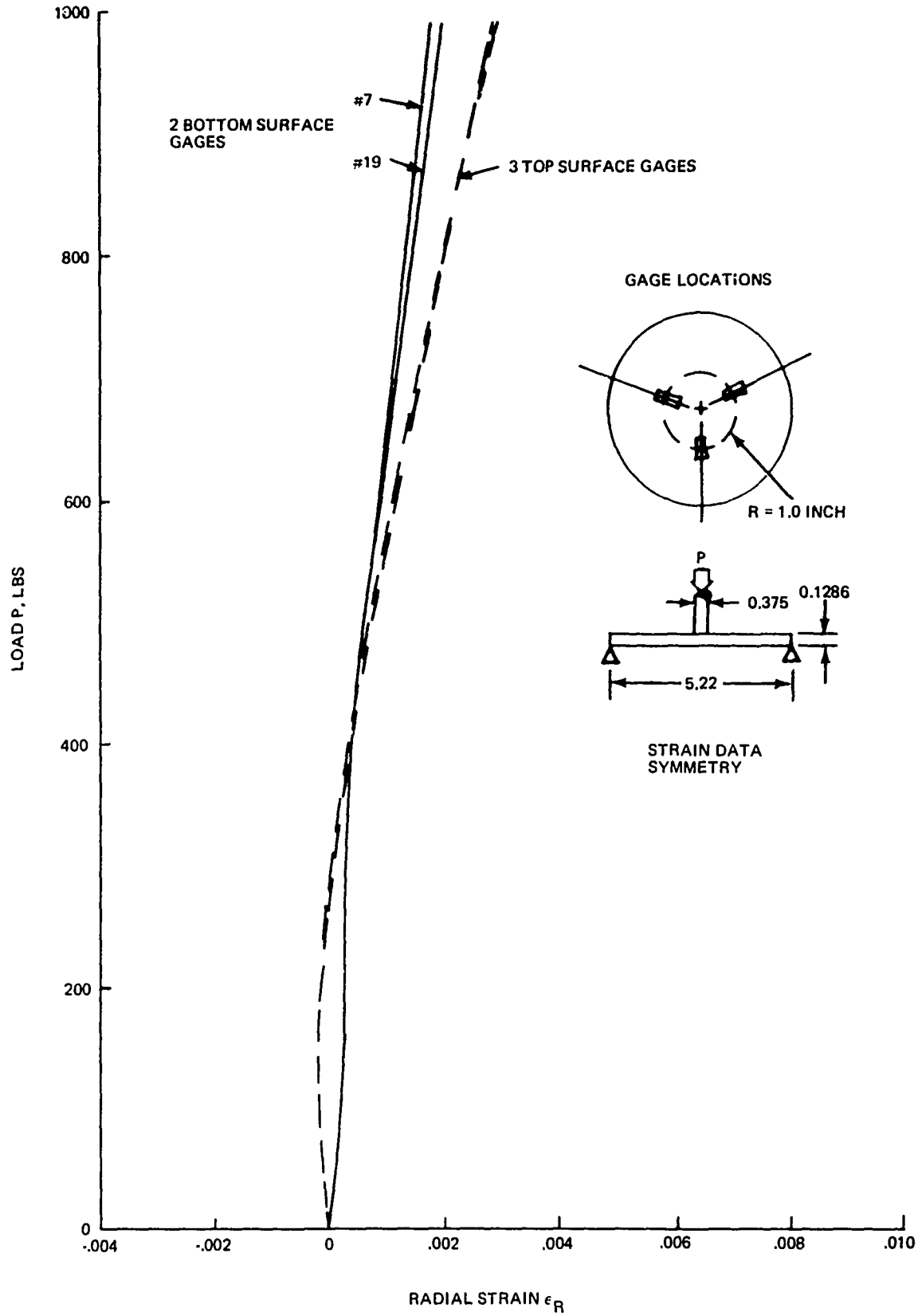

Fig. 24. Symmetry of Strain Data, Plate 4A125

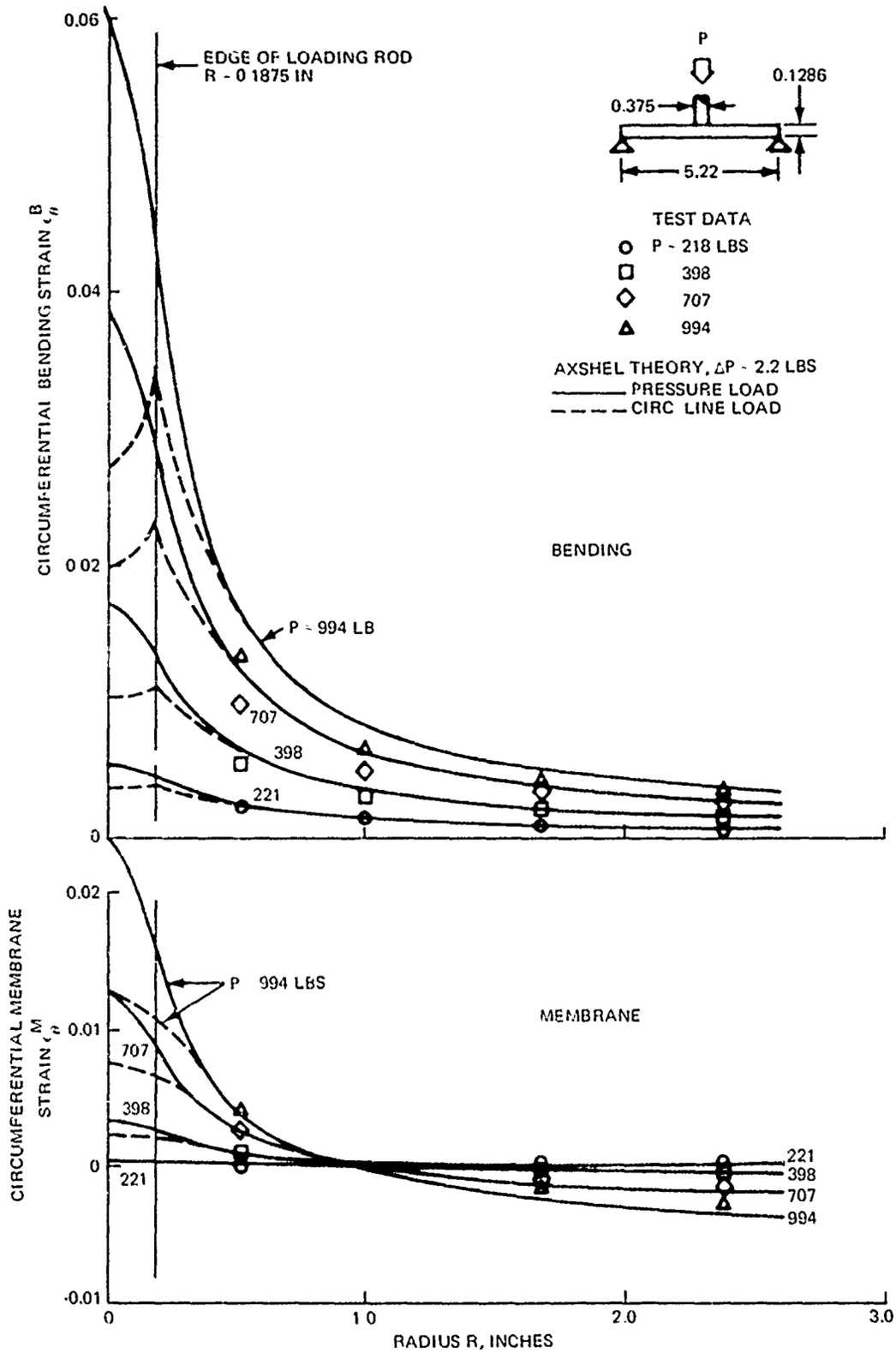

Fig. 25. Circumferential Bending and Membrane Strain Distributions, Plate #A1/5

strains. Such a plastic strain error would be greater for greater strain level, regardless of the mechanism, and could have been the main cause of the discrepancies.

If a comparison is made purely on the basis of strain level, it appears that the predictive error is about the same for the bending and membrane strains. However, the membrane strains at the gauge sites are not large enough to make this conclusion definite. Therefore, a clear judgment concerning the theoretical mechanism requiring improvement cannot be made at this time.

Some interesting behavior can be seen by comparing Figs. 25 and 22, and recalling that the lower surface strain at any point is the sum of the membrane and bending strains. It is known (Ref. 25, p. 415, for example) that the membrane strains in an initially flat elastic plate are approximately proportional to the square of the central deflection, during the early stages of the large deflection. Note that, as expected, the membrane strains were extremely small at low loads, but grew very rapidly with increasing load to become significant over the entire plate. The greatest membrane strains were in the central loaded region. In the outer half of the plate the membrane strains are not large, although they are significant compared to the bending strains. Near the outer edge, the compressive circumferential membrane strain was greater than the tensile bending strain and caused a strain reversal on the lower surface as the load increased (Figs. 21 and 22). Since the circumferential membrane strain was compressive outside a circle of approximate radius $R = 1$ inch, and since the membrane strain levels were increasing more rapidly than the bending levels, it seems safe to conclude that the strain reversal on the lower surface would have continued to spread inward to cover more of the plate.

This behavior is accounted for by the AXSHEL theory, by unloading along the elastic slope of the stress-strain curve at the points in question. Since the kinematic hardening rule is used, the elastic unloading may cover a stress range of up to twice the initial elastic limit in tension. This may result in a strain reversal, as reported here. In fact, AXSHEL will account for subsequent plasticity during the reversal, if the new elastic range is exceeded. This would be done by calculating the changes in plastic strain from the original stress-strain law, Eq. (1), but using reversed increments of stress and strain. This feature is discussed in more detail in Refs. 22, 23, and 24.

The test data and AXSHEL predictions for the $\frac{1}{4}$-inch thick plate 4A250, with $D/h = 20.0$, are shown in Figs. 26 through 31. The test was conducted to a maximum load of 4270 pounds, with a peak deflection approximately 1.6 times the thickness. The theory used 14 annular elements and load increments of 5.5 pounds, with both the uniform contact pressure and circular line load cases.

The load versus deflection data are plotted in Fig. 26, which again shows that the measured central deflection follows closer to the predicted deflections for the concentrated line loading than for the uniform contact pressure. The center LVDT recorded deformations almost equal to those of the load rod, up to approximately $w_o = 0.16$ inch $(w_o/h \approx 0.6)$, at which point the central LVDT reached its usable limit. The appearance of these curves has some similarity to that of the two $\frac{1}{8}$-inch plates, shown in Figs. 14 and 20, for equal w/h levels. In both cases the initial softening is followed by a gradual restiffening caused by membrane action under the large deflections. The main difference is that for the thicker plate of Fig. 26, the plastic deformation begins at a smaller value of w/h and the membrane restiffening occurs at a larger value of w/h than for the thinner plates.

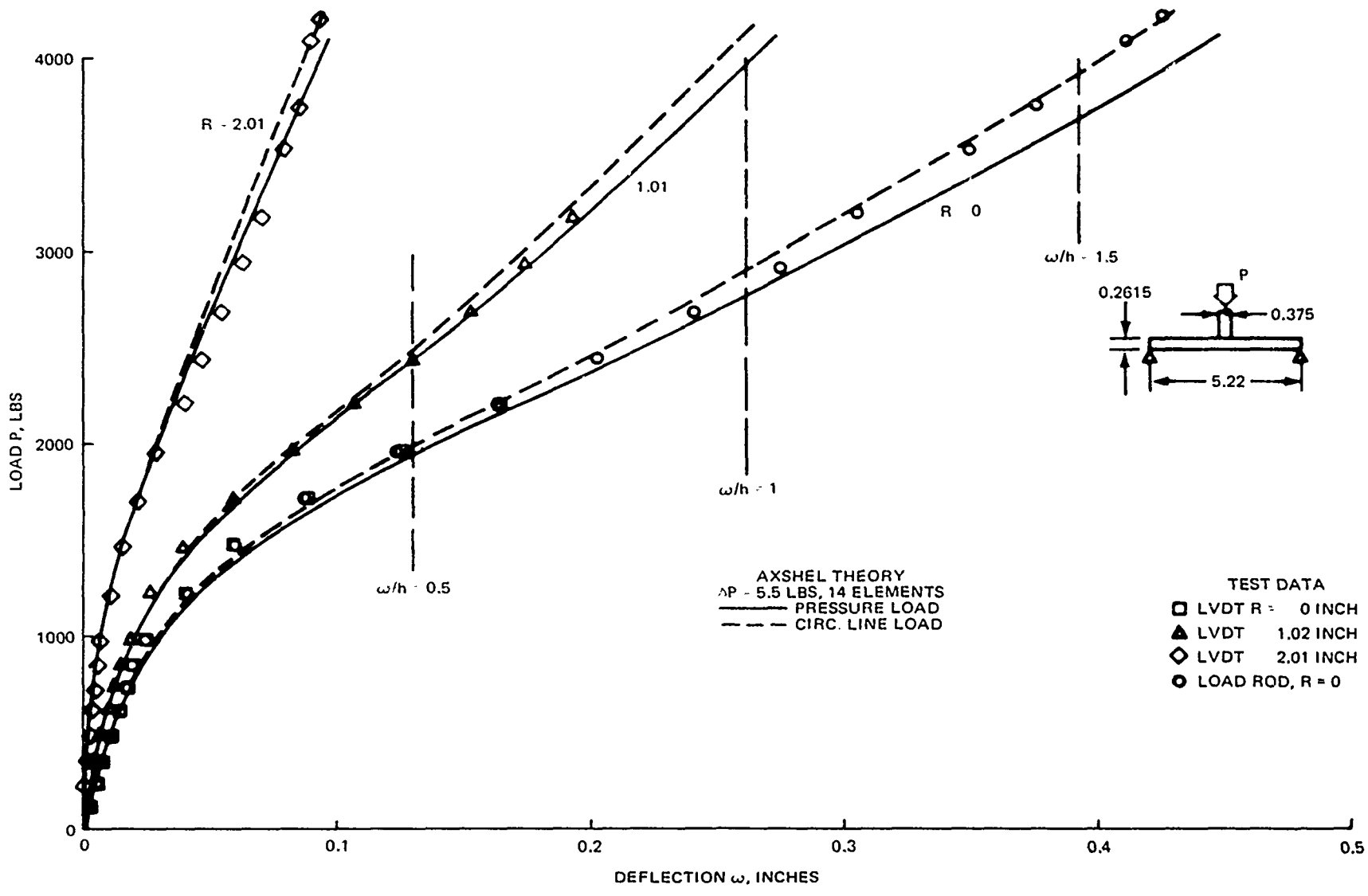

Fig. 26. Deflection History, Plate 4A250

The load versus strain data, plotted in Figs. 27 and 28, show that the theory was generally in good agreement with the measured values, except on the compression (top) surface near the plate center. The largest strain component was the tensile circumferential strain on the lower surface, for which the theory using the circular line load provided very good predictions, except at the center. This can best be seen in Fig. 29, where the circumferential strain distributions are plotted. The central strain measurement is between the predicted values for the two limiting cases of load distribution, but closer to the concentrated load case, as for the $\frac{1}{8}$-inch plate.

The radial strain distribution on the lower surface is plotted in Fig. 30, which exhibits the very local peak strains under the load concentration, that is typical of radial strains for this type of loading. An interesting feature is that the radial strain data remained nearly constant over most of the lower surface from 3200 to 4100 pounds load, but the theories predicted an increase. Note that the effect of the distribution of contact pressure was evident over an increasingly larger region of the plate, as the load increased.

The symmetry of strain was again better on the upper surface than the lower, as indicated by Fig. 31.

The membrane and bending strains were calculated from the test data according to Eqs. (2) and (3), and are plotted in Figs. 32 and 33. These are similar to those for the $\frac{1}{8}$-inch thick plates discussed, except that the load and strain levels are much higher. The sum of the bending and membrane strains (Figs. 32 and 33) equal the surface strain (Fig. 29). For this plate, the theoretical membrane strain predictions were lower in tension and greater in compression than the test data, effectively showing a compression shift relative

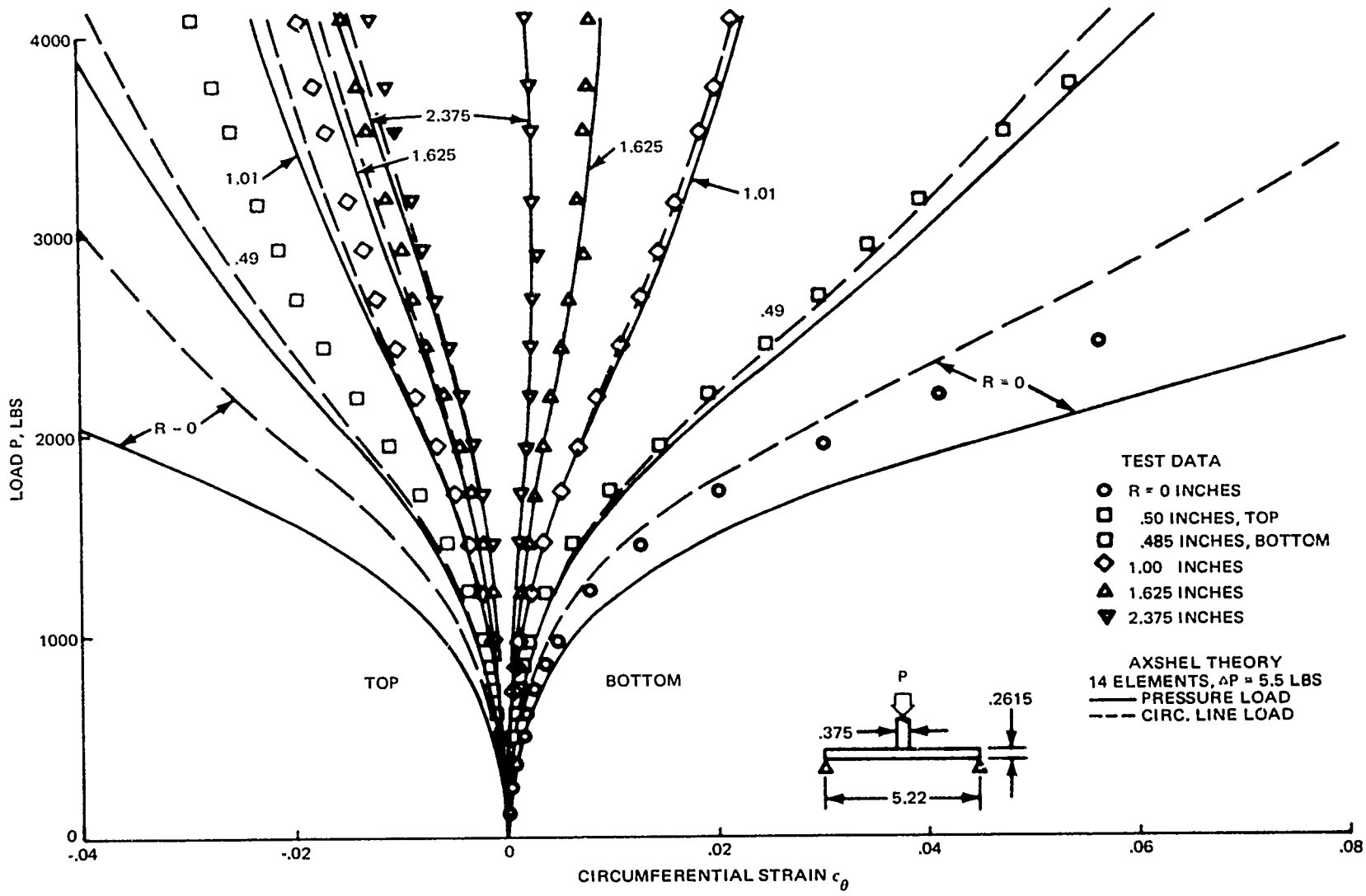

Fig. 27. Circumferential Strain History, Plate 4A250

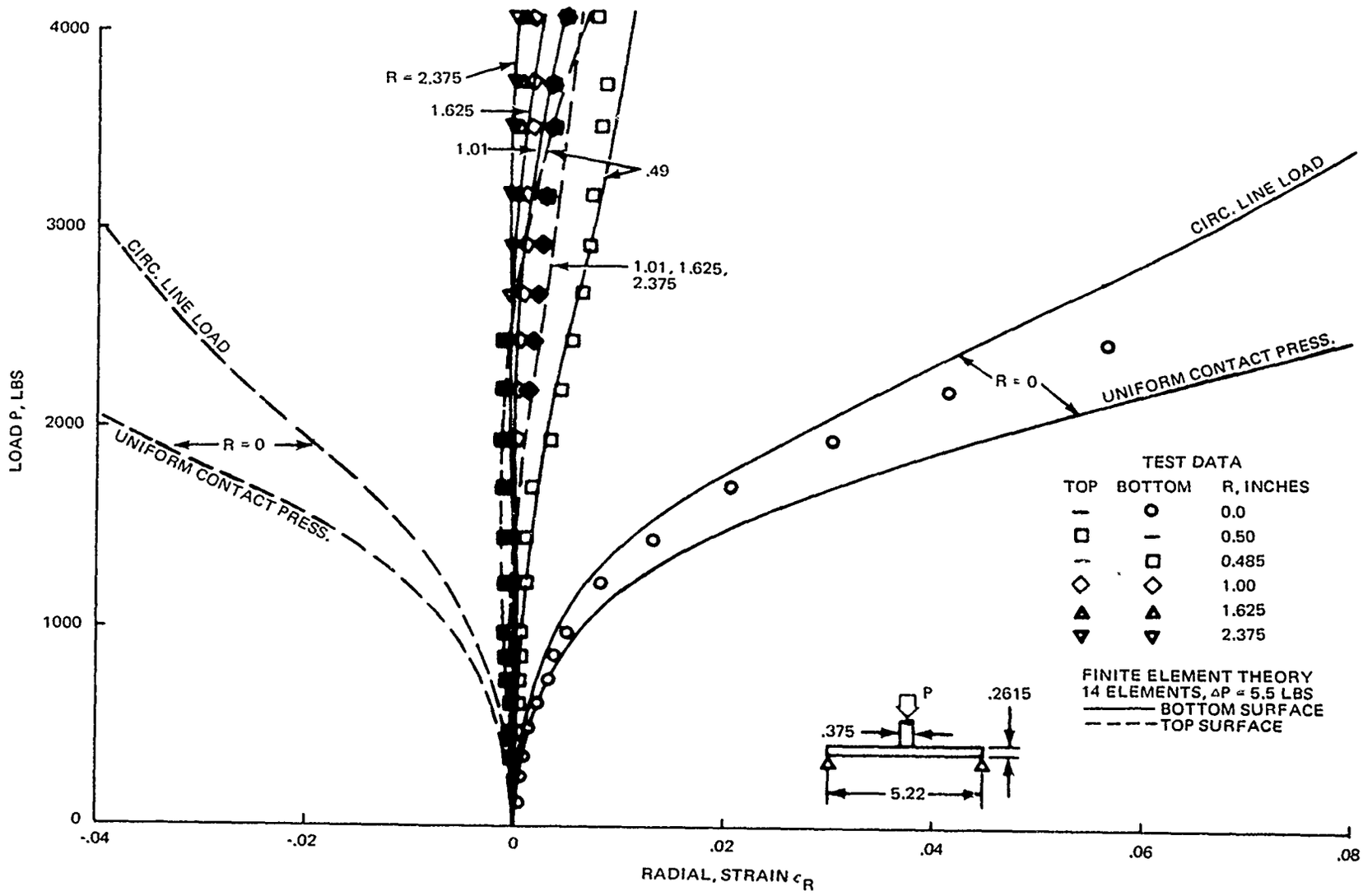

Fig. 28. Radial Strain History, Plate 4A250

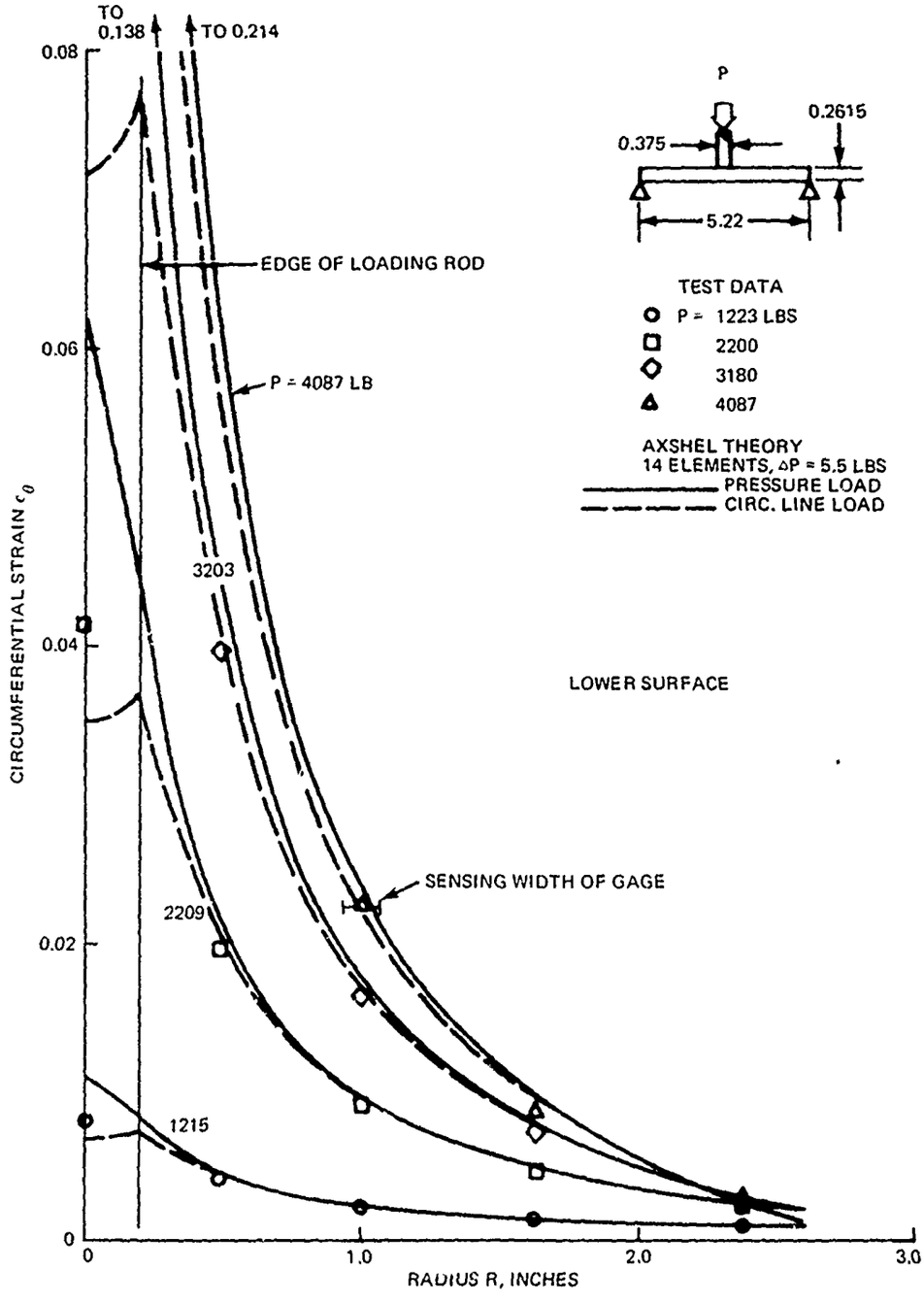

Fig. 29. Circumferential Strain Distributions, Lower Surface, Plate 4A250

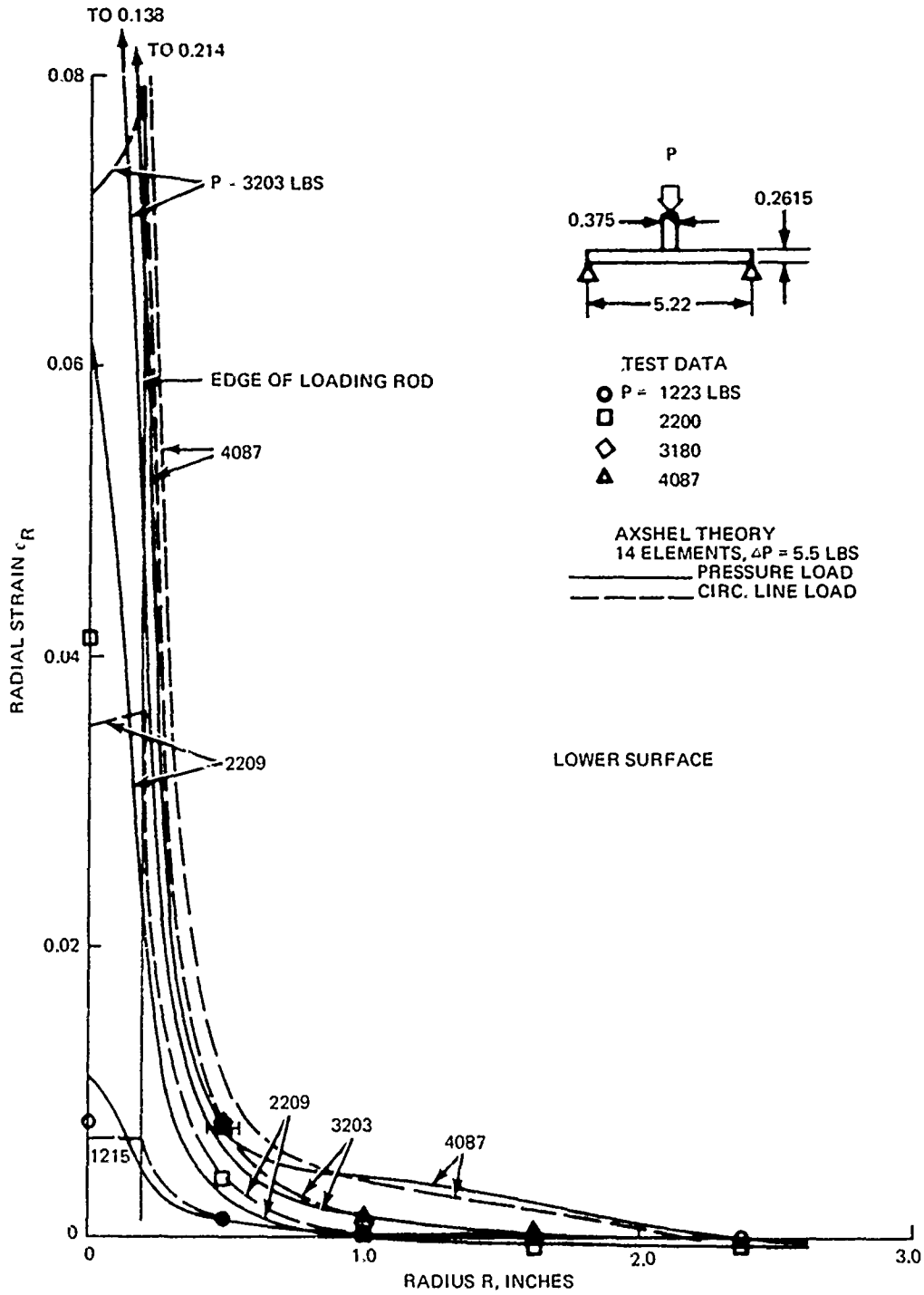

Fig. 30. Radial Strain Distributions, Lower Surface, Plate 4A250

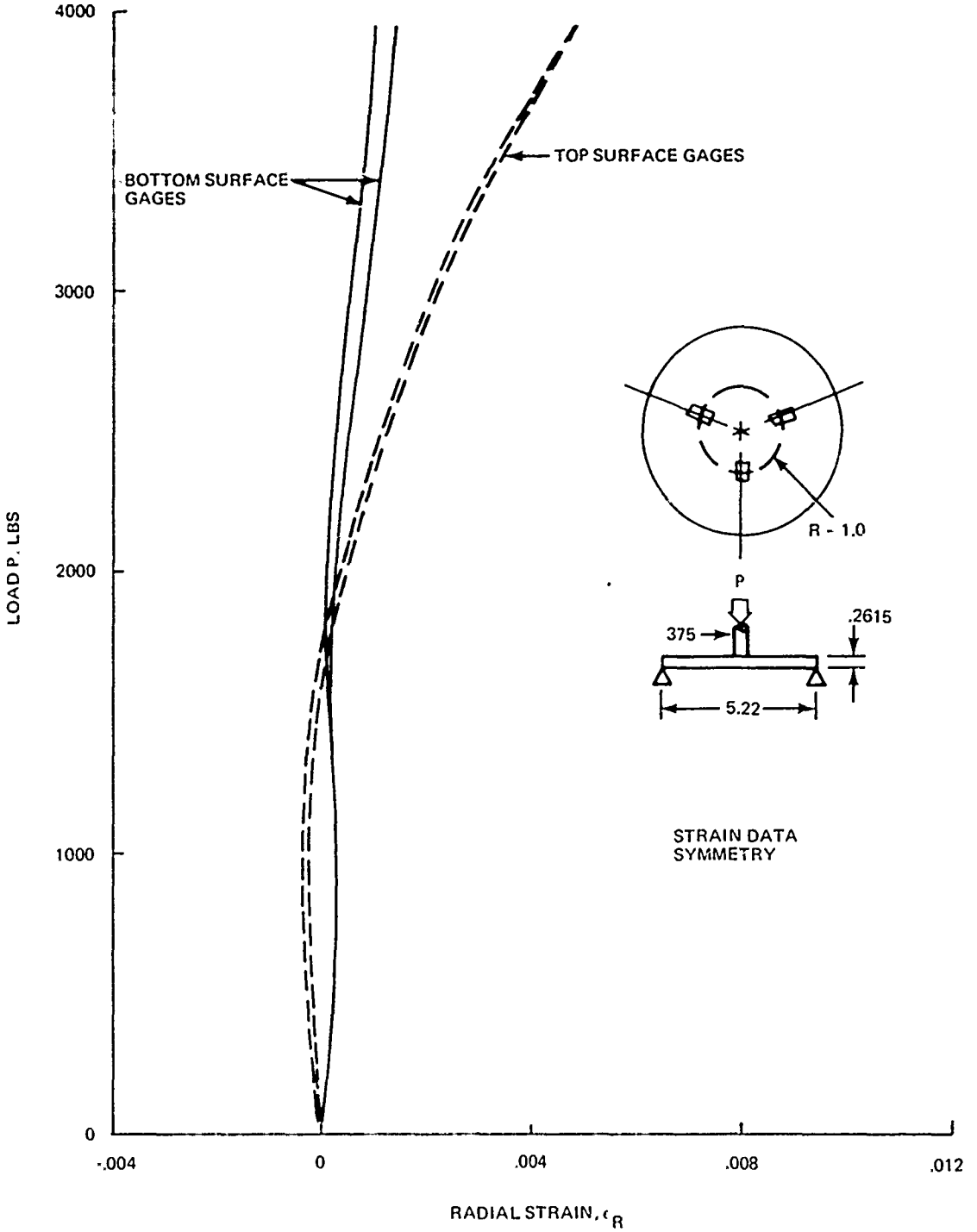

Fig. 21. Symmetry of Strain Data, Plate 4A250

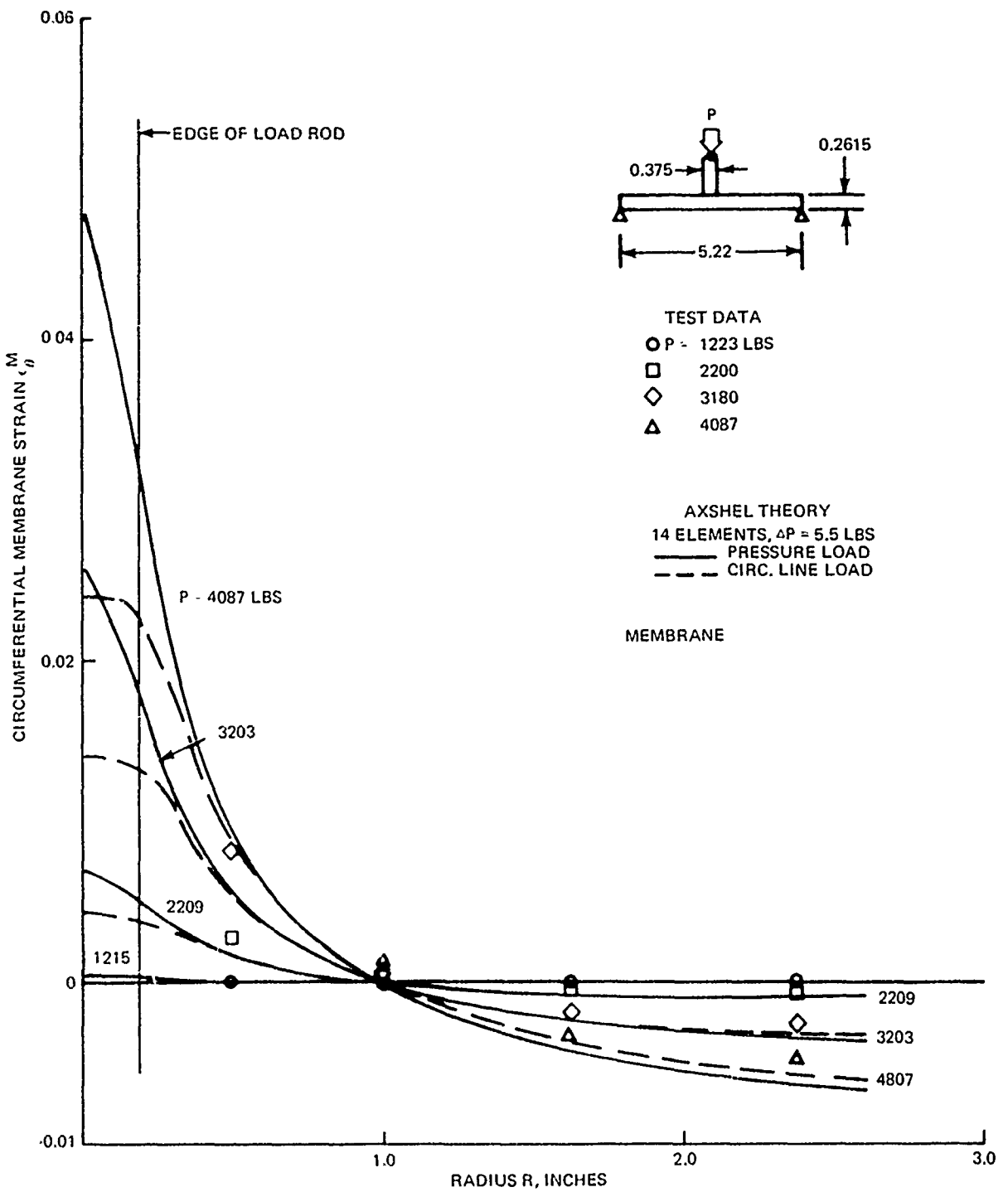

Fig. 32. Circumferential Membrane Strain Distribution, Plate 4A250

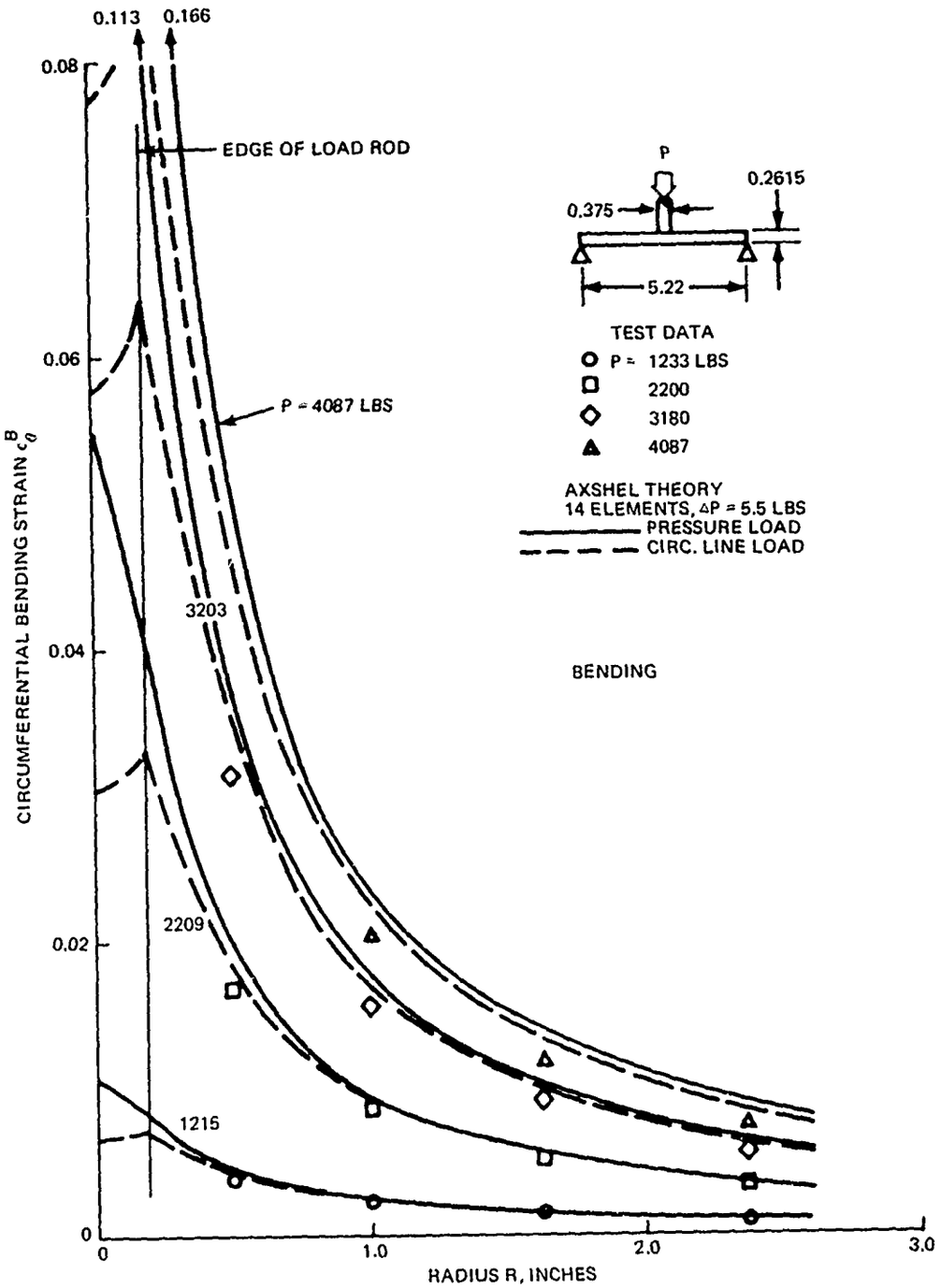

Fig. 33. Circumferential Bending Strain Distributions, Plate 4A250

to the test data. The bending strains show the opposite shift between test and theory, however. The net result was that the two predictive errors nearly canceled each other, producing the good correlation between test data and theory shown in Fig. 29. This was unique to the lower surface, since on the upper surface the bending strains reverse direction and then the two errors were additive, as can be seen in Fig. 27, which shows consistently poorer correlation on the top surface than on the bottom.

At the highest load, the effect of the theoretical contact pressure distributions upon the membrane and bending strains was spread across the entire plate, even to the outer edge. This was surprising, since it seemed reasonable to assume that away from the load rod, only the load level would determine the strains. Evidently this may not be true for cases of large nonlinear, plastic deformations. However, this effect may have been caused by the numerical procedures or the finite element approximations, so that using a greater number of elements might have eliminated these differences between the two results.

4. CONCLUSIONS

Test data from these three plates indicated that the qualitative aspects of the deflection and strain response were generally similar for the plates of diameter-to-thickness (D/h) ratios of 20.0 and 40.6. Initially, at lower loads, the plates developed a purely bending response, with plastic strains dominating in the circumferential direction. The radial plastic strains were large in the region of the load concentration at the plate centers. As the load increased, the stiffness (instantaneous slope of load versus deflection, $\Delta P/\Delta w_o$) decreased due to the spreading of the circumferential plastic bending strains over a larger region of the plates. At some point, the deflections became large enough to induce membrane strains, and brought membrane stiffness into effect. This occurred at a central deflection of approximately 40 percent of the thickness ($w_o/h = 0.4$). As the load increased, the membrane strains increased more rapidly than the bending strains, and the plate stiffness began to increase again at approximately $w_o/h = 0.8$. This trend of regaining stiffness was continuing when the tests were ended arbitrarily at about $w_o/h = 2.6$ for the thinner plates and $w_o/h = 1.6$ for the thicker plate, although the original elastic stiffness had not been reached. Evidently, as the load increased, the bending stiffness of the plate decreased while the membrane stiffness increased. This can be explained by considering that, for any given plate, the bending moments are primarily dependent on the load level and material rigidity, while the membrane forces depend primarily on the deflection and material rigidity. As the deflection induced by the bending action accelerates with load in the presence of material yielding, the membrane forces are induced and rise rapidly with load after plastic deformation becomes widespread. It is this increasing membrane action that

accounts for the apparent restiffening of the plate as the load increases.

The reason that these opposing mechanical trends can operate simultaneously in the same body is that the bending strains vary linearly through the thickness and are maximum near the surface, while the membrane strains are uniform through the thickness. Thus, while the surface yielding is spreading and is rapidly losing its resistance to the bending moments, the mid-plane region experiences only the smaller membrane strains with a more confined yielding area. Thus, the mid-plane membrane stiffness can still be increasing while the surface bending stiffness drops. However, some point must eventually be reached at which the mid-plane yielding will be so widespread that the over-all membrane stiffness must also begin to decline. Then the plate collapse will begin, with a final flattening of the slope of the load versus deflection curve, assuming that local fracture has not already occurred. This final yielding stage was not reached in the tests reported here, although it was reported by Sherbourne and Srivastava (Ref. 18).

The finite element theory used (the AXSHEL module of the Grumman-developed PLANS system) produced excellent predictions for the plate deflections, and generally good predictions for the strains. This was true in spite of the presence of severe strain gradients caused by localized loading. The predicted values of peak strain at the plate center, assuming a concentrated contact pressure on the edge of the loading rod, were about 10 to 15 percent under the measured strain values, for the larger load levels. This difference was attributed partly to the exact distribution of contact pressure under the loading rod being less concentrated than the assumed theoretical distribution and partly to the neglect of local contact stresses in the theory. Further improvement might be effected by incorporating an element with three dimensional stress

states into the AXSHEL module for use with load concentrations or abrupt changes in load distributions. This would allow for a more realistic estimate of the failure load, especially in cases where local fracture may precede ductile collapse.

Test data further showed that the need for including geometric nonlinearity effects (large deformations and membrane forces) in the theory was even more important than expected. This is because these effects became significant shortly after the onset of plastic deformations.

5. REFERENCES

1. Way, S., "Bending of Circular Plates with Large Deflection," Trans. ASME, Vol. 56, pp. 627-636, 1934.

2. McPherson, A., Ramberg, W., and Levy, S., "Normal Pressure Tests of Circular Plates with Clamped Edges," NACA Report 744, 1942

3. Ramberg, W., McPherson, A., and Levy, S., "Normal Pressure Tests of Rectangular Plates," NACA Tech. Note 849, 1942.

4. Naghdi, P., "Bending of Elastoplastic Circular Plates with Large Deflection," J. Appl. Mech., ASME, pp. 293-300, September 1952.

5. Haythornthwaite, R., "Deflection of Plates in the Elastic-Plastic Range," Second U.S. Nat. Congr. Appl. Mech., pp. 521-526, 1954.

6. Cooper, R. and Shifrin, G., "Experiment on Circular Plates in the Plastic Range," Second U.S. Nat. Congr. Appl. Mech., pp. 527-534, 1954.

7. Haythornthwaite, R. and Onat, E., "The Load Carrying Capacity of Initially Flat Circular Steel Plates under Reversed Loading," J. Aeronaut. Sci., Vol. 22, No. 12, pp. 867-869, December 1955.

8. Foulkes, J. and Onat, E., "Tests of Behavior of Circular Plates under Transverse Load," Brown U., Div. of Engineering Report OOR 3172/3, May 1955.

9. Olszak, W. and Sawczuk, A., "Experimental Verification of Limit Analysis of Plates, Part I," Bull. l'Acad. Polonaise des Sciences, Cl. IV, Vol. III, No. 4, pp. 195-200 (in English), 1955.

10. Onat, E. and Haythornthwaite, R., "Load Carrying Capacity of Circular Plates at Large Deflection," J. Appl. Mech., ASME, Vol. 23, pp. 49-55, March 1956.

11. Lerner, S. and Prager, W., "On the Flexure of Plastic Plates," J. Appl. Mech., ASME, pp. 353-354, June 1960.

12. Lance, R. and Onat, E., "Comparison of Experiments and Theory in the Plastic Bending of Circular Plates," J. Mech. Phys. Solids, Pergammon Press, Ltd., Vol. 10, pp. 301-311, 1962.

13. Ohashi, Y. and Murakami, S., "The Elasto-Plastic Bending of a Clamped Thin Circular Plate," Proc. 11th Int. Cong. Applied Mechanics, Munich, pp. 212-223, 1964.

14. Ohashi, Y. and Murakami, S., "Large Deflection in Elastoplastic Bending of a Simply Supported Circular Plate under a Uniform Load," J. Appl. Mech., Trans. ASME, pp. 866-870, December 1966.

15. May, G., "Elastic Plastic Behavior of Plates," U. of Colorado, Ph.D. Thesis, 1967. University Microfilms, Ann Arbor, Michigan.

16. Ohashi, Y. and Kawashima, K., "On the Residual Deformation of Elasto-Plastically Bent Thin Circular Plate after Perfect Unloading," Zeitschrift Ang. Math. Mek. (in English), Vol. 49, No. 5, pp. 275-286, 1969.

17. Srivastava, N. and Sherbourne, A., "Elastic Plastic Bending of Circular Plates," J. Engineering Mechs. Div. ASCE, pp. 13-31, February 1971.

18. Sherbourne, A. N. and Srivastava, N. K., "Elastic-Plastic Bending of Restrained Pin-Ended Circular Plates," Int. J. Mech. Sci., Vol. 13, pp. 231-241, 1971.

19. Durelli, A. J., Parks, V. J., and Chen, T. L., "Elastoplastic Analysis of a Bent Plate with a Circular Hole," Soc. Exp. Stress Anal. Spring Meeting, Salt Lake City, Utah, Paper No. 1822, May 1971.

20. Portevin, S. and LeChatelier, M. A., "Sur un Phenomene Obs rve Lors de l'Essai de Traction d'Alliages en Cours de Transformation," Comptes Rendus Acad. Sci. Paris, Vol. 176, pp. 507-510, 1923.

21. Bodner, S. R. and Rosen, A., "Discontinuous Yielding of Commercially Pure Aluminum," J. Mechs. Phys. Solids, Vol. 15, pp. 63-77, 1967.

22. Armen, H., Levine, H., Pifko, A., and Levy, A., "Nonlinear Analysis of Structures," NASA CR-2351, 1974.

23. Pifko, A., Levine, H. S., Armen, H., and Levy, A., "PLANS - A Finite Element Program for Nonlinear Analysis of Structures," ASME publication 74-WA/PVP-6, Winter Annual Meeting, New York, November 1974.

24. Pifko, A., Levine, H. S., and Armen, H., "PLANS - A Finite Element Program for Nonlinear Analysis of Structures. Vol I - Theoretical Manual," Grumman Research Department Report RE-501, April 1975; to be published as a NASA CR.

25. Timoshenko, S. and Woinowsky-Krieger, S., Theory of Plates and Shells, McGraw-Hill Co., 1959.

26. Anderson, C. A. and Shield, R. T., "On the Validity of the Plastic Theory of Structures for Collapse under Highly Localized Loading," J. Appl. Mech., Trans. ASME, pp. 629-636, September 1966.

APPENDIX A

STRAIN GAUGE CONFIGURATION

The factory-installed copper terminals of the strain gauges can be seen best in Fig. 8 (Gauges 15, 17, and 21), and are connected to the gauge foil by flexible horizontal loops that are supposed to mechanically isolate the solder terminals from the gauge to provide a longer fatigue life. A series of exploratory tests was performed to compare the peak usable strain level of these gauges having the factory-installed terminals with that of three altered gauge configurations, as follows:

- Configuration 1: Unmodified. Full carrier area and factory-attached copper jumpers and solder tabs
- Configuration 2: Copper jumpers removed, single strand wire jumper used
- Configuration 3: Same as 1, plus carrier and cement trimmed close around copper jumper
- Configuration 4: Same as 2, plus carrier and cement trimmed close to gauge element

Configuration 2 is a common hand-worked gauge installation technique, which configuration 1 was designed to replace.

Three special 2024-0 aluminum tension coupons were made, each one having bonded to it four gauges. These gauges were one each of the four configurations described above. The primary purpose of these exploratory tests was to determine if configuration 1 could perform as well as the standard method, configuration 2. The other configurations were added to see if any further improvement could be affected.

The results of these tests were that the single-strand jumper, configuration 2, sustained the highest average failure strain, about 9.5 percent, with configuration 1 close behind at 8.2 percent. The others performed relatively poorly, in the 4 to 5 percent range. It was decided that the convenience and labor-saving features of the factory-installed tabs and jumpers more than offset the slightly lower failure strain, and all the strain gauges used in this project were of the configuration 1 type.

APPENDIX B

STRAIN GAUGE DATA PROCESSING

Tension Tests

Strain gauge data processing was setup to correct the gauge data for known systematic errors. Data were corrected by means of the formula

$$\epsilon/\epsilon' = \alpha\beta \tag{B-1}$$

in which ϵ is the corrected strain, ϵ' the indicated strain, and α and β are the correction factors for transverse sensitivity and bridge nonlinearity.

The transverse sensitivity correction was (Ref. B.1)

$$\alpha = (1 - 0.285k)/[1 + (\epsilon_T'/\epsilon')k] \tag{B-2}$$

where k is the manufacturer's stated transverse sensitivity factor and ϵ_T' is the indicated transverse strain. This formula is derived from the fact that the manufacturer's gauge specifications are determined from calibration tests using steel bars having a Poisson's ratio of 0.285. For tension coupons with dual gauge sets, having transverse gauges, the value of α was recalculated for each measurement. For tension coupons with single gauges, without transverse gauges, the substitution

$$\epsilon_T'/\epsilon' \equiv -\mu \tag{B-3}$$

was made, where μ was the elastic Poisson's ratio. Note that in the special case of large transverse strains when $\epsilon'/\epsilon_T' \approx -k$, the value of α blows up, and Eq. (B-2) cannot be used. In that case, α was interpolated linearly from the strain readings before and after the instability. This condition appeared occasionally with dual gauge sets in the plate tests.

The bridge nonlinearity correction was (Ref. B.2)

$$\beta = 1 + 0.5\ G\epsilon' \qquad \text{(B-4)}$$

where G is the manufacturer's stated gauge factor. This correction was required to compensate for the slightly nonlinear output of the single active arm type of circuit used for these tests.

The extensometer strain was calculated by dividing the indicated extension by the initial gauge length. Figure B-1 shows the remaining error of the strain gauge data, relative to the extensometer strain, after correcting by means of Eq. (B-1). Note that the residual strain gauge error was negative. That is, the corrected gauge data were smaller than the extensometer data, and that the average error magnitude is slightly less than the nominal strain level. Although the scatter in the gauge error was large, the overall average error shows a systematic trend which could have been represented mathematically and included as another factor in Eq. (B-1). This was not done primarily because the causes of this remaining error were unknown and it was uncertain how this error would be affected by the bidirectional strain states in the circular plate specimens. Therefore, it was decided not to make use of Fig. B-1 in correcting the strain gauge data for either the tension coupons or the plate specimens, so that the true stress-strain curves developed from the tension data were corrected in the same way as the strain data reported for the plate tests.

Plate Tests

For the plate tests, the strain gauge data were corrected for transverse sensitivity and bridge nonlinearity errors as described under tension tests. An additional correction was made to compensate for the fact that the radially and circumferentially oriented

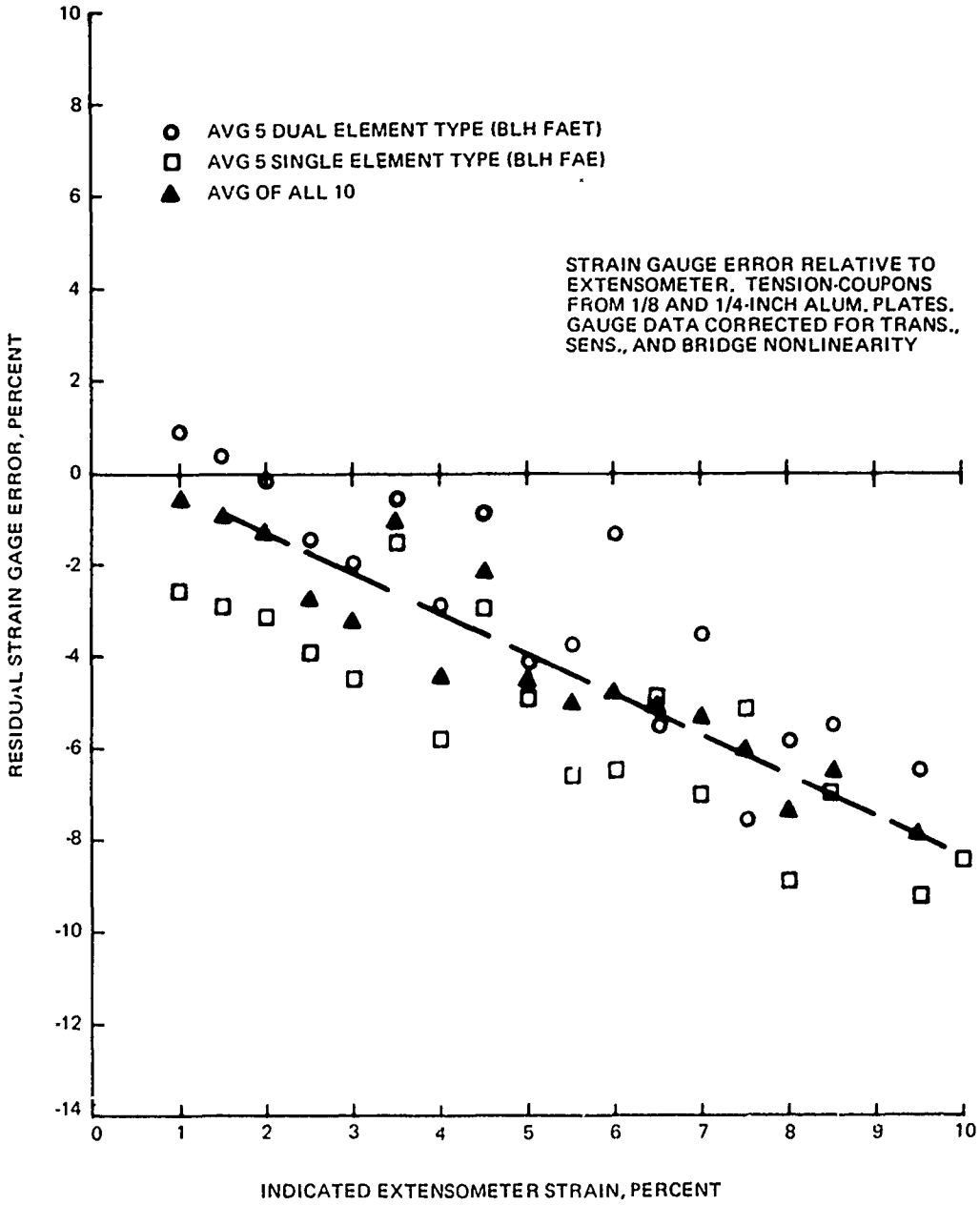

Fig. B-1. Strain Gauge Error After Certain Corrections

gauge sets had a slight rotational misalignment with respect to the true radial and circumferential directions, as shown in Fig. B-2. This was a consequence of the requirement that the dual gauge sets be installed so that both gauges in a set would be at the same radial distance from the center.

If the gauge centers are apart by a distance 2δ, then the misalignment angle is

$$\Phi = \text{arc sin}(\delta/R) \tag{B-4}$$

Given the two strain measurements at right angles to each other, and assuming the plate behavior to be perfectly symmetric so that any two gauges on the same circle can be considered to be at the same point, Mohr's circle equations can be used to calculate the strains in the exact radial and circumferential directions.

In Fig. B-2, the "radial" gauge on the left is rotated an angle $-\Phi$ from the actual radial position, while the gauge on the right is an angle $+\Phi$ from the actual circumferential position. The Mohr's circle for this case is shown in Fig. B-3. Note that the actual strains, ϵ_r and ϵ_θ, are principal strains, and that it does not matter if the gauge positions are reversed (dashed lines in Fig. B-3). The indicated strains, ϵ_r' and ϵ_θ' are

$$\epsilon_r' = \tfrac{1}{2}(\epsilon_r + \epsilon_\theta) + \tfrac{1}{2}(\epsilon_r - \epsilon_\theta) \cos 2\Phi \tag{B-5}$$

$$\epsilon_\theta' = \tfrac{1}{2}(\epsilon_r + \epsilon_\theta) - \tfrac{1}{2}(\epsilon_r - \epsilon_\theta) \cos 2\Phi \tag{B-6}$$

or

$$\epsilon_r' = \tfrac{1}{2}(1 + \cos 2\Phi)\epsilon_r + \tfrac{1}{2}(1 - \cos 2\Phi)\epsilon_\theta \tag{B-7}$$

$$\epsilon_\theta' = \tfrac{1}{2}(1 + \cos 2\Phi)\epsilon_\theta + \tfrac{1}{2}(1 - \cos 2\Phi)\epsilon_r \tag{B-8}$$

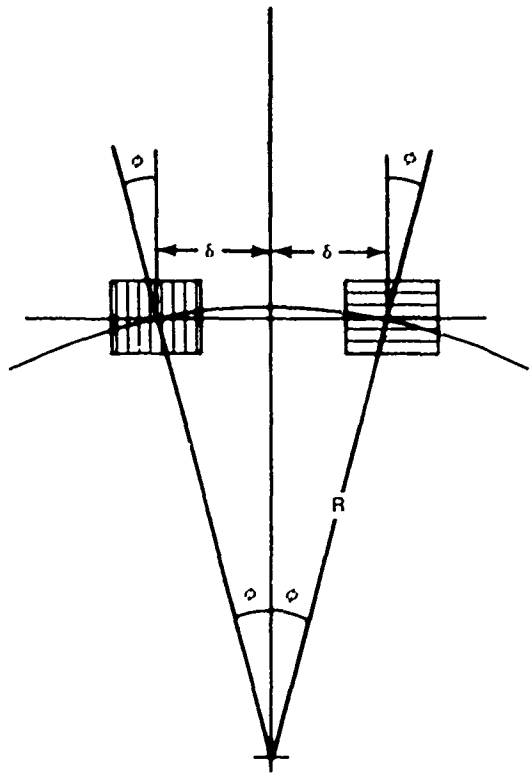

Fig. B-2. Strain Gauge Alignment Geometry

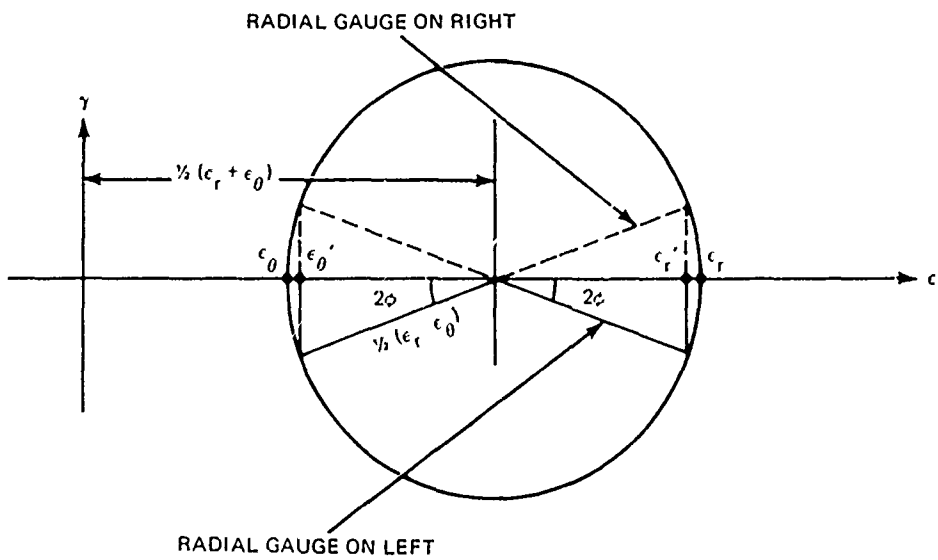

Fig. B-3. Mohr's Circle for Strain Gauge Alignment Error Analysis

Since $1 + \cos 2\phi = 2\cos^2\phi$ and $1 - \cos 2\phi = 2\sin^2\phi$, these become

$$\epsilon_r' = \cos^2\phi\,\epsilon_r + \sin^2\phi\,\epsilon_\phi \tag{B-9}$$

$$\epsilon_\phi' = \cos^2\phi\,\epsilon_\phi + \sin^2\phi\,\epsilon_r \tag{B-10}$$

Solving for the actual strains, get

$$(\cos^2\phi - \sin^2\phi)\epsilon_r = \epsilon_r' \cos^2\phi - \epsilon_\phi' \sin^2\phi \tag{B-11}$$

$$(\cos^2\phi - \sin^2\phi)\epsilon_\phi = \epsilon_\phi' \cos^2\phi - \epsilon_r' \sin^2\phi \tag{B-12}$$

But from Eq. (B-4),

$$\sin^2\phi = (\delta/R)^2 \tag{B-13}$$

$$\cos^2\phi = 1 - (\delta/R)^2 \tag{B-14}$$

and Eqs. (B-11) and (B-12) become

$$[1 - 2(\delta/R)^2]\epsilon_r = [1 - (\delta/R)^2]\epsilon_r' - (\delta/R)^2\epsilon_\phi' \tag{B-15}$$

$$[1 - 2(\delta/R)^2]\epsilon_\phi = [1 - (\delta/R)^2]\epsilon_\phi' - (\delta/R)^2\epsilon_R' \tag{B-16}$$

Thus for any gauge, the correction factor is

$$\gamma = \epsilon/\epsilon' = \left[\frac{1 - (\delta/R)^2}{1 - 2(\delta/R)^2}\right] - \left[\frac{(\delta/R)^2}{1 - 2(\delta/R)^2}\right]\epsilon_T'/\epsilon' \tag{B-17}$$

where ϵ' is the indicated strain of the gauge, and ϵ_T' is the indicated strain of the gauge transverse to it. This applies to both the radial and circumferential gauges.

For the experiments described here, $\delta = 0.070$ inch and the minimum R was 0.5 inch, so that the maximum δ/R was 0.14. In that case a good approximation to Eq. (B-17) can be derived by replacing the bracketed terms by infinite series, and dropping terms in $(\delta/R)^3$ or higher powers. The result is

$$\gamma = 1 + (\delta/R)^2 - (\delta/R)^2 \epsilon_T'/\epsilon' \qquad \text{(B-18)}$$

Thus, the complete correction equation for the plate tests was

$$\epsilon/\epsilon' = \alpha\beta\gamma \qquad \text{(B-19)}$$

where α and β were defined previously, and γ comes from Eq. (B-18).

References

B.1 Wu, C. T., "Transverse Sensitivity of Bonded Strain Gauges," Exp. Mechs., Vol. 2, pp. 338-344, November 1962.

B.2 Anon., "Errors Due to Wheatstone Bridge Nonlinearity," Tech. Note 139, Micro-Measurements Inc., Romulus, Michigan.

APPENDIX C

TRUE STRESS CALCULATIONS

For the stress-strain curves, the true stress P/A (load over current cross section area) was calculated from the engineering stress P/A_o (load over initial area) by

$$\sigma = \frac{P}{A} = \frac{P}{A_o}\frac{A_o}{A} = \frac{P/A_o}{(1 + \epsilon_T)^2} \tag{C-1}$$

where ϵ_T is the current strain transverse to the loading axis. The ϵ_T is related to the longitudinal strain ϵ, by

$$\epsilon_T = -\mu\epsilon \tag{C-2}$$

where μ is Poisson's ratio. This leads to

$$\sigma = \frac{P/A_o}{(1 - \mu\epsilon)^2} \tag{C-3}$$

which can be approximated by

$$\sigma \approx (1 + 2\mu\epsilon)P/A_o \tag{C-4}$$

In the absence of other data, it is common practice to set $\mu = 0.5$ in the plastic range, which gives a true stress of

$$\sigma \approx (1 + \epsilon)P/A_o \tag{C-5}$$

In the tests described here, the stress-strain data from the $\frac{1}{4}$-inch plate material were processed by hand. To save time, formula (C-5) was used. For the $\frac{1}{8}$-inch plate material, however, the data were processed by a digital computer program especially made for this purpose. The true stress values were calculated using Eq. (C-1) when transverse gauges were installed, and Eq. (C-3) otherwise. An effective value of $\mu = 0.33$ was used with Eq. (C-3), as this was close to the average effective value of Poisson's ratio

in the plastic range, calculated by the computer from the transverse gauge data.

APPENDIX D

THEORETICAL MODEL

A system of computer codes is being developed at the Grumman Aerospace Corporation, called PLANS (Plastic Large deflection ANalysis of Structures) which predicts the mechanical response of loaded structures into the inelastic range of material behavior, using the finite element method of numerical structural analysis. The PLANS system treats elastic-plastic material behavior by using the Von Mises yield criterion in conjunction with the kinematic hardening rule of plastic flow. Geometric nonlinearities, that is, alterations in structural characteristics caused by shape changes under load, are also accounted for in certain modules of PLANS by updating geometric and stiffness properties in a piecewise linear fashion. The structures are modeled by the finite element method, which replaces the actual body by a number of smaller simply shaped bodies, or elements, connected at their mutually adjacent surfaces. Since the elements are relatively simple in shape, the mathematical model for the deformations and strains in each element type can be found, or approximated, and a complex structure can be approximated by an assemblage of many simple elements. Since there is a separate set of equations for each element, the total number of simultaneous equations to be solved is generally large, requiring use of matrix analysis techniques in conjunction with a high speed digital computer.

The nonlinear behavior, caused by both material plasticity and shape changes, is calculated by a series of incremental linear approximations. As the load is increased by a small increment, the corresponding increments of deformation, strain, stress, etc., are calculated using the currently effective stiffness characteristics

of each element, as known at the start of each increment. Since these effective element stiffnesses are lagging slightly behind the true stiffnesses, the prediction for each increment will be slightly in error. As the previous incremental solutions are added up to produce the current total predicted state of the structure, this small incremental error will accumulate and increase as the load level increases. However, the accumulated error can be reduced by using smaller load increments or by performing certain corrections.

Since the finite element model assembly is an approximation to the actual structure, the accuracy of the model can also be increased, up to a point, by using more elements of smaller size.

A description of the PLANS system, its theoretical basis, and its operation is described in Refs. 22, 23, and 24.

The plates tested here were analyzed using the AXSHEL module of PLANS. This module handles axisymmetric thin shells or thin plates, using annular elements. The element behavioral equations use a shell theory which includes the effects of bending moments, membrane forces, and large deflections. Not included in this theory are the effects of transverse shear, transverse normal stresses, and the local contact stresses in the region of a load concentration.

The particular finite element models used for each plate are shown in Fig. D.1. Either a 14-annular element or a 27-annular element configuration was used, although there were slight variations among the same basic configurations used for the different plates. These models differed from the actual case primarily in that the loading was assumed to be either a uniform pressure inside the loading circle, or a concentrated load on the circumference of the circle, while the actual loading was provided by a flat-ended hard steel circular rod with an unknown distribution of contact

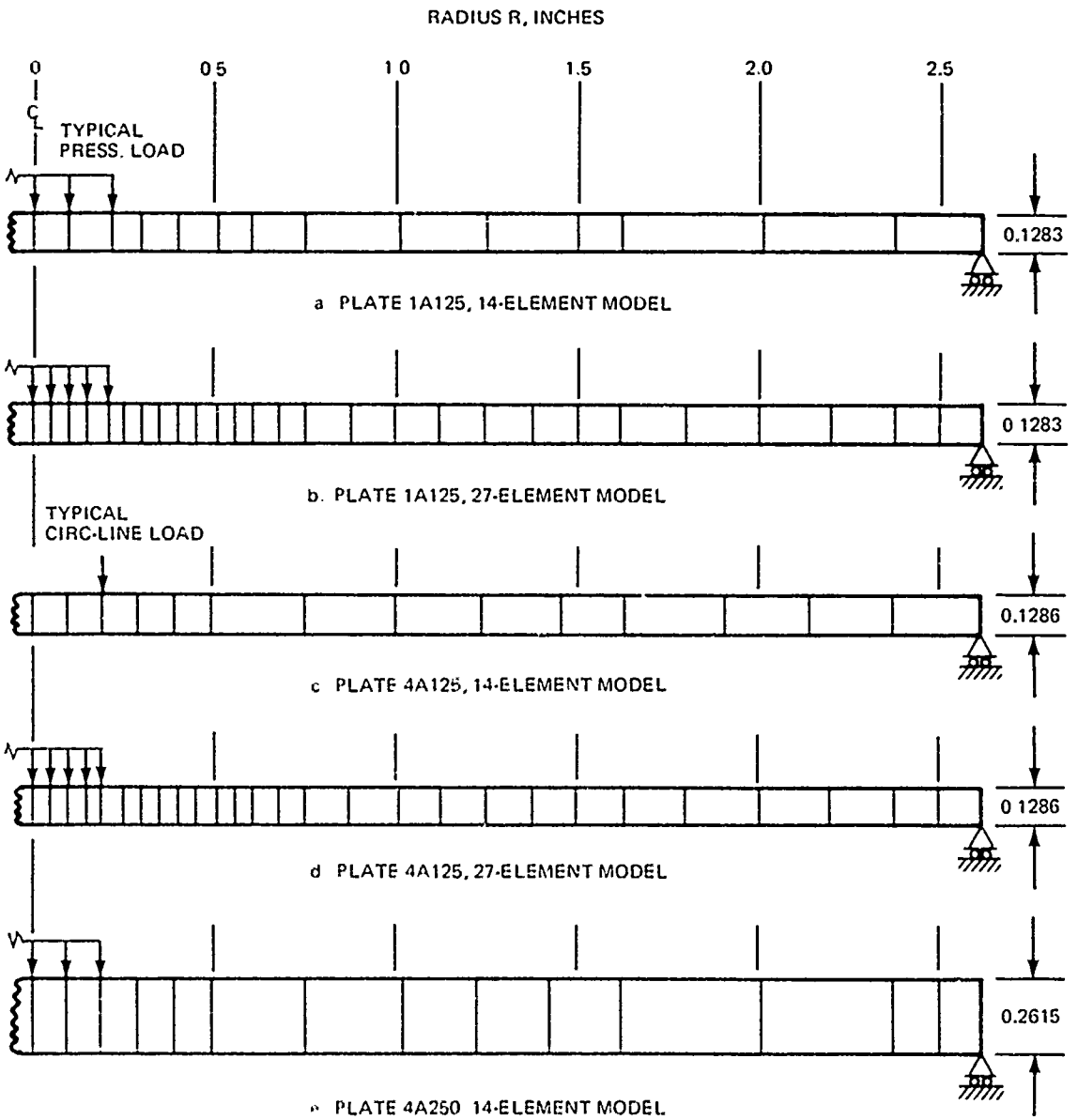

[illegible] Cross-Section View

pressure. The distribution of pressure inside the load circle was expected to vary as the plate deformed under load. Another deviation of the model was that the actual plate was slightly larger in diameter than the support circle by about 0.063 inch, but this overhang was not accounted for in the model.